GRK 1782

"Functionalization of Semiconductors"

Seminar 2021

Tagungshaus Schloss Herborn, 22.09.2021 – 24.09.2021

Research Summaries

supported by: Deutsche Forschungsgemeinschaft

Graduiertenkolleg 1782
“Functionalization of Semiconductors”
Tagungshaus Schloss Herborn

Program 22. – 24.09.2021

Wednesday, 22.09.2021

until 12:00	Arrival
12:15 – 12:55	Lunch
	Session I
13:30 – 14:00	***Marcel Kröner***: Investigation of Ga(P,Sb) towards a possible direct Band Gap
14:00 – 14:30	***Thilo Hepp****:* Bismuth containing W-type laser structures for long wavelength emission on GaAs
14:30 – 15:00	Coffee Break (Dining Hall)
	Session II
15:00 – 15:30	***Johannes Glowatzki***: MOVPE Growth of SiGe at Low Growth Temperatures and p-doping via Ga Incorporation
15:30 – 16:00	***Robin Günkel****:* In-situ analysis of Ga(As,Bi) interfaces during low temperature growth by MOVPE
16:00 – 16:30	***Christian Ritter****:* Interpnictogen MOVPE Precursors
16:30 – 18:00	Move into the rooms, possibility for scientific exchange in small groups
18:15 – 18:50	Dinner

Thursday, 23.09.2021

07:15 – 07:50	Breakfast
	Session III
09:00 – 09:30	***Tobias Dunaj (Posterpräsentation)***: Synthesis of Binary Interpnictogen Compounds from Diaryl and Dimethyl Halido Bismuthanes
09:30 – 10:00	***Luise Rost***: The influence of excitation power and temperature on the luminescence properties and offset of Ga(As,Sb) and (Ga,In)As-based type II heterostructures
10:00 – 10:30	Coffee Break
	Session IV
10:30 – 11:00	***Maximilian Widemann***: In-situ TEM Investigations of III/V Semiconductor Materials
11:00 – 11:30	***Mikko Wilhelm***: Optoelectronic Coupling between Colloidal Quantum Dots and Semiconductor Substrates
11:30 – 12:00	***Florian Kreuter***: Surface functionalization with nonalternant aromatic compounds: a computational study of azulene and naphthalene on Si(001)
12:15 – 12:55	Lunch
13:30 – 17:30	**Discussions** Networking - Joint nature hike around Herborn: Kleiner Wäller "Hessentagswanderweg"
18:15 – 18:50	Dinner

Friday, 24.09.2021

07:15 – 07:50	Breakfast
08:00 – 09:00	Tidy up and leave rooms
	Session V
09:00 – 09:30	***Badal Mondal***: Strain induced direct-indirect transition in ternary III-V semiconductor from ab-initio approach
09:30 – 10:00	***Oliver Maßmeyer***: MOVPE growth of Ga(N,As) interlayers with high N contents on GaAs (001) surfaces
10:00 – 10:30	Coffee Break
	Session VI
10:30 – 11:00	***Saleh Firoozabadi***: Quantification of light elements at a low angular regime; a combination of EFSTEM and 4DSTEM
11:00 – 11:30	***Sven Christian Liebscher***: High-Harmonic Generation in Tellurium
12:15 – 12:55	Lunch
afterwards	Departure

Speaker's research summaries

(in order of schedule)

Investigation of Ga(P,Sb) towards a possible direct Band Gap

M. Kröner[1], P. Ludewig[2], J. Zimmet[2], S. Reinhard[1], W. Stolz[1,2]

[1]Department of Physics and Materials Sciences Center, Philipps-University Marburg
[2]NasP III/V GmbH

Introduction

One of the big challenges in Si based optoelectronics (OEIC) is the realisation of a stable and efficient laser integrated on exact Si (001) substrate. In order to achieve an efficient light source grown lattice matched to Si (001), a direct band gap semiconductor is required. In this work the ternary III-V semiconductor Ga(P,Sb) is investigated towards its properties. In first growth experiments Jou et al. (1988)[1] found a direct nature of the band gap of Ga(P,Sb) for Sb-concentrations of 32 % and higher. For lower concentrations they concluded from their results that this semiconductor becomes indirect and any observed luminescence is due to donor-acceptor pair recombination. Russell et al. (2016)[2] investigated this material system more recently using diffuse reflectance ultraviolet-visable spectroscopy (UV-Vis) and density functional theory (DFT). They claim a direct nature of the respective band gap for Sb-concentrations as low as 1 % and above.

Results

Since Ga(P,Sb) is compressively strained with respect to the Si lattice constant, the approach in this work is the metalorganic vapor phase epitaxy (MOVPE) of thin QW-layers < 10 nm of Ga(P,Sb) between (B,Ga)P bulk layers. The (B,Ga)P layers help for the strain compensation on the Si (001) substrate as well as in the carrier confinement for luminescence experiments. Growth was performed at 575 °C using tri-ethyl-gallium (TEGa), tri-ethyl-antimony (TESb), tertiary-butyl-phosphine (TBP) and di-borane (B_2H_6) as precursors at various V/III-ratios from 10 to 20.

Sb-concentrations of up to 17.5 % could be achieved for reasonable QW-thicknesses (Fig. 1 (a)). The Sb-incorporation efficiency clearly drops for higher Sb-supplies (Fig. 1 (a) green asterisks) as is expected, since Sb is known to segregate to the samples surface during growth. Also, even higher Sb-concentrations would further increase the compressive strain and reduce the critical thickness for the layered, defect free growth. The strong modulation of the respective X-ray diffractograms indicate well defined interfaces of the Ga(P,Sb) QWs (Fig. 1 (b)). Although a high structural quality of MQW-heterostructures could be obtained, PL measurements at 78 K with excitation at 405 nm wavelength shows weak and broad luminescence of only two structures with the lowest Sb-concentrations 5 % and 8 % at 1.73 eV and 1.63 eV peak energy, respectively. Samples with higher Sb-incorporation exclusively show broad luminescence of the Si-substrate around 1.1 eV. Measured band gaps and band bowing is shown for several publications in Fig. 1 (d).

Conclusions & Outlook

The measured luminescence at 78 K exhibits low overall intensity and shows broad linewidths although a very high structural quality with low defect densities could be achieved. This leads us to the conclusion, that a direct nature of the band gap of Ga(P,Sb) for Sb-concentrations up to 17.5 % as suggested by Russell et al. (2016) cannot be confirmed but rather fits to the indirect band gap and donor-acceptor pair recombination as suggested by Jou et al. (1988). The investigated material system does therefore not serve as an efficient light source in the respective composition range grown pseudomorphically on Si (001) substrates.

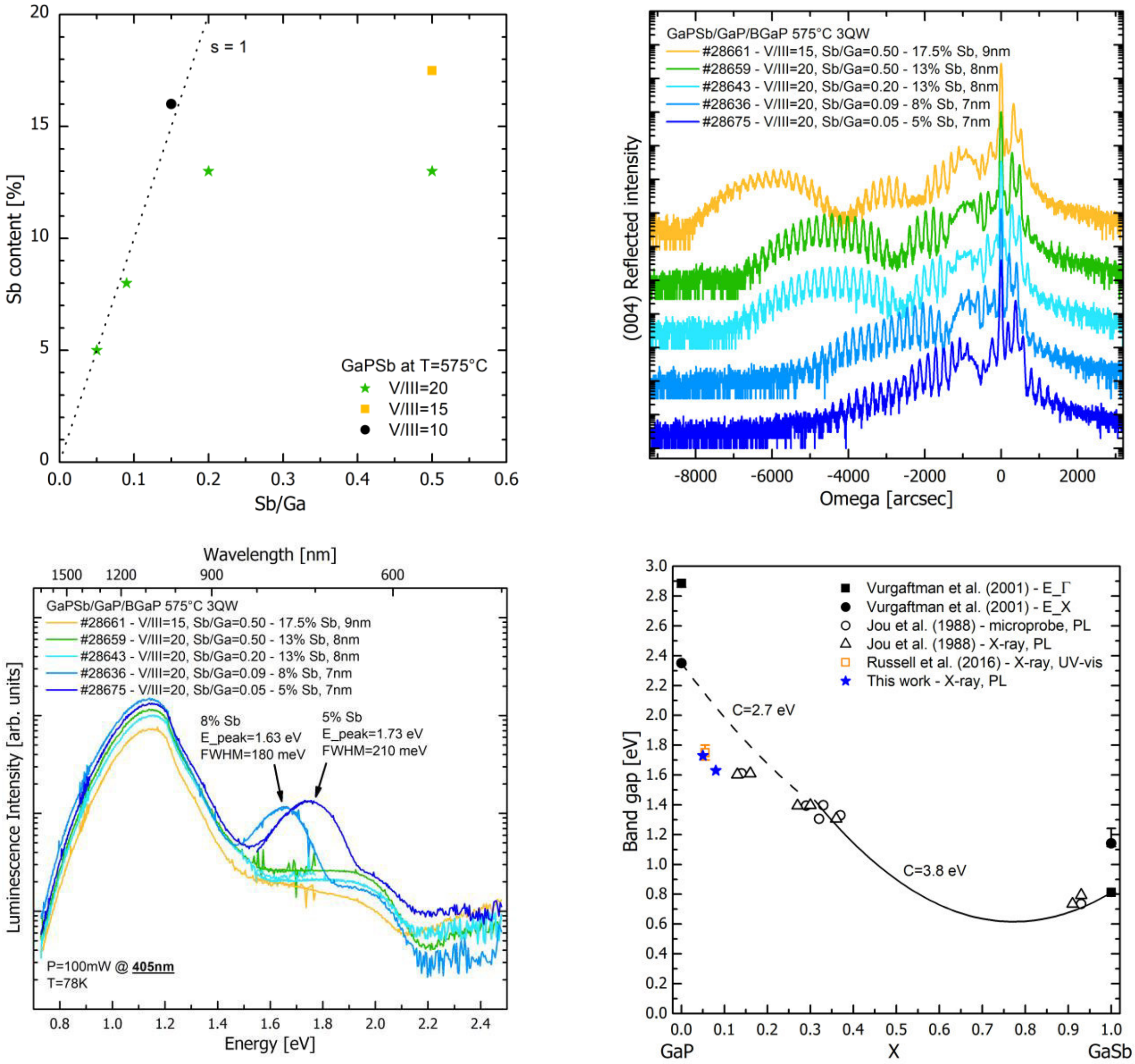

Fig. 1: (a) Sb-incorporation in Ga(P,Sb). (b) X-ray diffractograms of several Ga(P,Sb)/(B,Ga)P MQW-heterostructures. (c) PL-spectra at 78 K. (d) Band gap versus composition for several publications[1-3] and this work.

References

[1] M. J. Jou, Y. T. Cherng, H. R. Jen and G. B. Stringfellow, “Organometallic Vapor Phase Epitaxial Growth of a new Semiconductor Alloy: $GaP_{1-x}Sb_x$”, App. Phys. Lett. 52, 549-551 (1988).

[2] H. B. Russell, A. N. Andriotis, M. Menon, J. B. Jasinski, A. Martinez-Garcia and M. K. Sunkara, “Direct Band Gap Gallium Antimony Phosphide ($GaSb_xP_{1-x}$) Alloys”, Sci. Rep. 6, 20822 (2016).

[3] I. Vurgaftman, J. R. Meyer and L. R. Ram-Mohan, “Band Parameters for III-V Compound Semiconductors and their Alloys”, J. App. Phys. 89, 5815-5875 (2001).

Bismuth containing W-type laser structures for long wavelength emission on GaAs substrates

T. Hepp[1], R. Günkel[1], O. Maßmeyer[1], J. Glowatzki[1], S. Chatterjee[2] and K. Volz[1]

[1]Materials Sciences Center and Department of Physics, Philipps-University Marburg, Germany
[2]Institute of Experimental Physics I, Justus-Liebig-University Gießen, Germany

In this work we will present the growth and room temperature laser operation of (Ga,In)As/Ga(As,Bi)/(Ga,In)As W-type structures (WQW) grown on ex. GaAs (001). The growth peculiarities will be tackled and the necessary steps to realize this kind of heterostructure will be discussed. Moreover, we will discuss our first results on laser structures based on (Ga,In)As/Ga(As,Bi)/(Ga,In)As WQWs as active region.

Promising results have been archived for (Ga,In)As/Ga(As,Sb)/(Ga,In)As WQWs[1], however, the laser emission beyond 1.3 µm is prevented by strain limitations. Ga(As,Bi) is a promising candidate to replace Ga(As,Sb) in these structures since Bi incorporation shows a strong increase in valance band energy. More important, the shift of the valance band per mole fraction is increased compared to Sb incorporation. Due to the high mismatch in size and electronegativity, compared to As species, localized defect states are introduced below the valance band edge of the GaAs host material upon Bi incorporation. This results in a restructuring of the valance bands described by the so-called band anti-crossing model. In this model the valance bands (heavy hole, light hole and spin-orbit split-off band) split, which results in a drastic reduction of the band gap. An enormous valance band shift by about 53 meV/%Bi is found and additionally the conduction band is shifted downwards by about 28 meV/%Bi. Hence, in theory it is possible to shift the emission wavelength of (Ga,In)As/Ga(As,Bi)/(Ga,In)As WQWs further into the mid infrared region as with the counterpart (Ga,In)As/Ga(As,Sb)/(Ga,In)As.

Sample growth is conducted in an AIXTRON AIX 200 horizontal reactor system. Triethylgallium (TEGa), trimethylindium (TMIn), tertiarybutylarsane (TBAs), and trimethylbismuth (TMBi) are chosen as precursors. Structural analysis in order to determine layer thicknesses and compositions is carried out by utilizing high resolution X-Ray diffraction (HR-XRD). Electrical characterization is carried out using pulsed excitation of 400 ns current pulses with a repetition rate of 10 kHz. The optical output is recorded by a Ge detector. The sample surface is investigated using an atomic force microscope (AFM) in tapping mode.

A schematic of the (Ga,In)As/Ga(As,Bi)/(Ga,In)As WQW band structure is shown in Fig. 1 a): The charge carriers are separated in two adjacent layers. The electrons are confined in the (Ga,In)As layers while the holes are confined in the Ga(As,Bi) layer. The second (Ga,In)As QW is required for significant wave function overlap of the holes and electrons. It is also possible to embed one (Ga,In)As layer by two Ga(As,Bi) layers, which is considered as a M-structure. However, in this case the gain, which is important parameter for laser devices would decrease[2].

The rather complex growth sequence of the sample that is required to deposit the layer stack with high epitaxial quality and smooth interfaces is shown in Fig. 1 b). The necessity of the different steps and the optimization process will be discussed in the presentation.

With the sophisticated growth sequence, it is possible to control the interface formation despite the segregation of In and Bi on the growth surface. In previous experiments combined segregation of In and Bi facilitate droplet formation in contrast to solely Bi segregation[3]. From these structures laser devices have been fabricated and investigated in terms of electrical and luminescence properties.

Room temperature laser operation is confirmed by measurement of the light-current characteristic shown in Fig. 2 a). A threshold current density (J_{TH}) of 4.13 ± 0.50 kA/cm^2 is determined. The optical efficiency (η_λ) is determined to 0.092 ± 0.014 W/A per facet. An electroluminescence spectra recorded at threshold of this particular laser stripe shows the emission wavelength of 1040 nm.

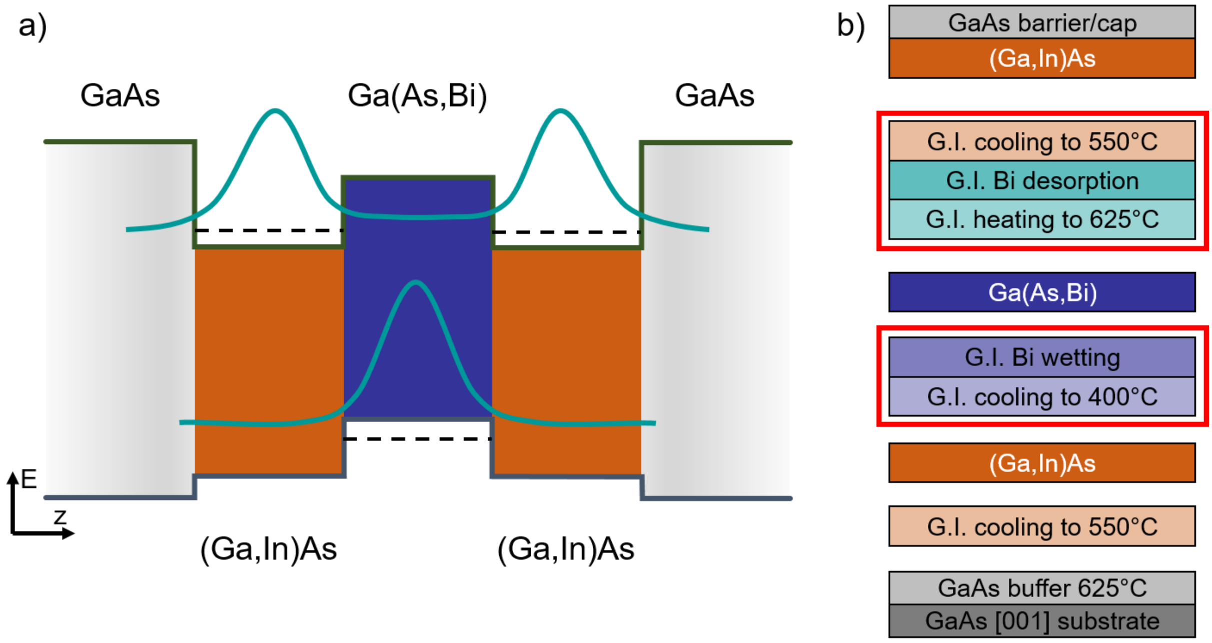

Fig. 1: a) Shows a sketch of the band structure of a (Ga,In)As/Ga(As,Bi)/(Ga,In)As WQW including the electron wave function. The electron and holes are confined in the (Ga,In)As and Ga(As,Bi) layers, respectively. b) The growth sequence of the WQW is depicted. The important steps are the growth interruptions introduced at the interfaces, which are marked by the red boxes.

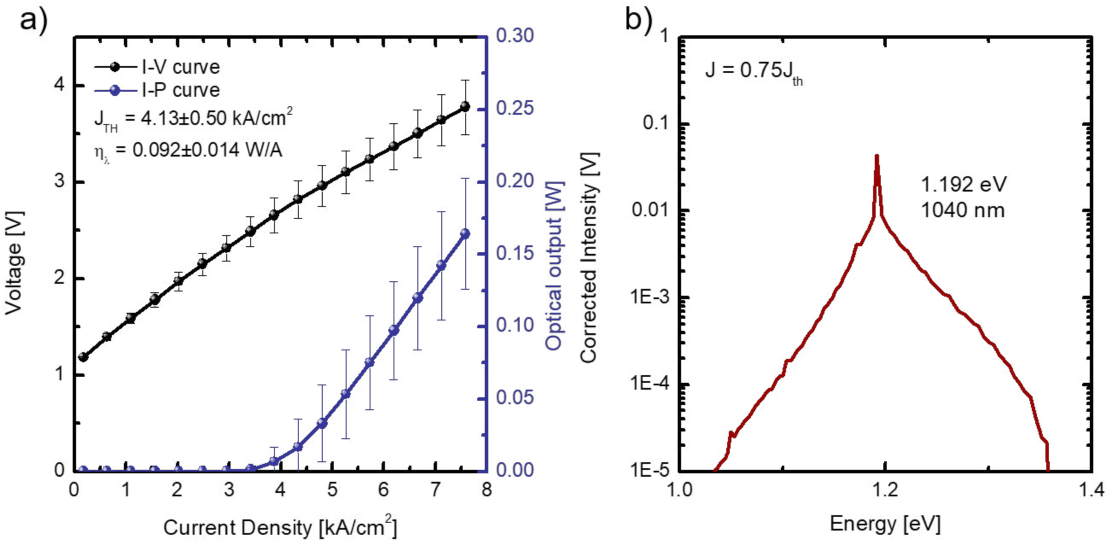

Fig. 2: A plot of the I-V and I-P curve is shown in a). It is clearly visible, that the device reaches threshold and begins lasing operation at a current density of around 4.13 kA/cm^2. In b) electroluminescence measurement carried out right below threshold shows the laser emission at 1040 nm.

References

[1] C. Fuchs et al., Sci. Rep. 8 (1), 8-13 (2018)
[2] C. Wang et al., Chin. Phys. Lett. 35 (5), 057801 (2018)
[3] T. Hepp et al., J. Appl. Phys. 126, 085707 (2019)

MOVPE Growth of SiGe at Low Growth Temperatures and p-doping via Ga Incorporation

J. Glowatzki, H. Abouarab, T. Hepp, O. Maßmeyer, K. Volz

Materials Sciences Center and Department of Physics, Philipps-University Marburg, Germany

Introduction

CMOS technology is miniaturized into the tens of nm regime for improving the energy consumption and also the cost per calculation unit. With miniaturization the relative losses are increased due to the contact resistivity of the source and drain and lowering of this value is of significant importance. P-type SiGe is often used as material for source/drain regions. Since B doping seems not to be sufficient for reaching contact resistivity values that are low enough research is carried out for other/additional dopants. Experiments using implantation and laser annealing showed that Ga doped and also Ga/B co-doped SiGe reach lower contact resistivity values compared to B and they seem also sufficient to fulfill the future technology nodes[1]. First experiments have been carried out for in-situ co-doping of B and Ga during SiGe epitaxy[2]. A main issue seems to be the C incorporation and also the segregation of Ga during the epitaxy. In the results part the main focus will be on the growth of SiGe using disilane and digermane as precursors. Furthermore, first Ga doping experiments will be presented.

Results and Conclusions

In Fig. 1 first results on the growth of SiGe at low growth temperatures are shown. Fig. 1 a) shows the growth rate dependence of SiGe with a Ge content between 50 - 55 % and a strong increase in growth rate with growth temperature is visible which is slower increasing at higher temperature until 500 °C. An explanation could be the higher H passivation of the active sites on the Si surface during growth at lower temperatures. With increasing temperature, the H can desorb and the surface is more active which results in higher growth rate. In Fig. 1 b) – d) it is clearly visible that while the disilane offer is increasing at fixed digermane offer, the growth rate is decreasing at every investigated growth temperature. This effect can probably be explained by enhanced H passivation due to the strong binding of H to Si. The effect of decreasing growth rate with disilane offer is getting weaker with increasing growth temperature. This fits to the assumption of decreasing hydrogen passivation with increasing growth temperature.

In Fig. 2 results of the first experiments to the Ga doping experiments of SiGe are shown. Fig. 2 a) shows the Ga SIMS profile for various SiGe:Ga/SiGe structures. Sample structures can be seen in the inlet in figure 2 b). For three different growth temperatures and Ge compositions around 50 % it is clearly visible that the Ga is segregating during the growth to the surface and an increase in incorporation can be seen for higher growth temperatures. This segregation effect is not visible for the sample grown at 400 °C. The segregation can be suppressed using such low growth temperatures. In Fig. 2 b) the C SIMS profiles of the same samples can be seen. For every sample the C incorporation seems to be under 1E18 cm^{-3} which is the background limit of the measurements. So TTBGa seems to be a good candidate as precursor for low Ga segregation and low C incorporation.

In the talk further results on the growth of SiGe at low temperatures and experiments to increase the Ga incorporation will be shown.

References

[1] L.-L. Wang et al. 2017, IEEE International Electron Devices Meeting (IEDM), pp. 22.4.1-22.4.4

[2] C. Porret et al. 2019, ECS Journal of Solid State Science and Technology 8 (8), P392-399

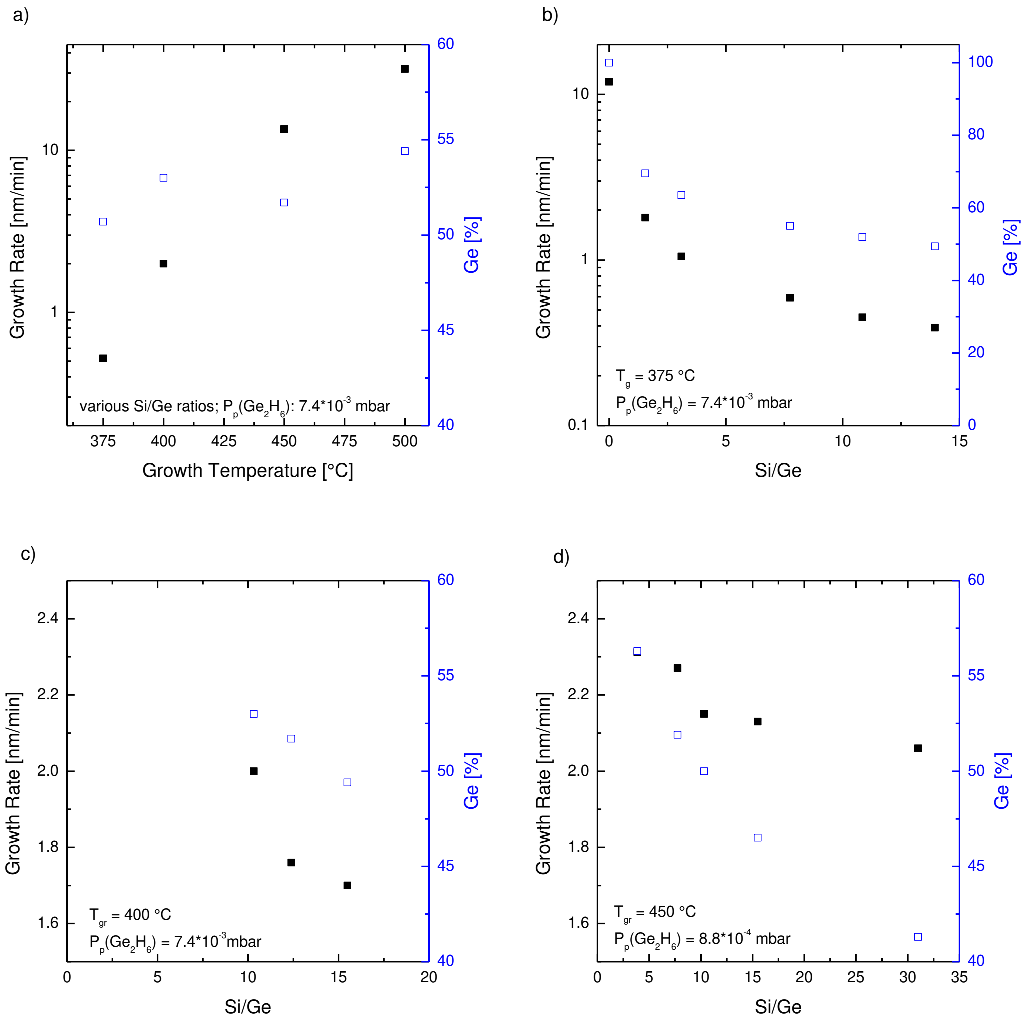

Figure 1: In a) the growth rate and Ge incorporation for different growth rates are shown. In b) - d) the growth rate and Ge incorporation at fixed digermane offer and varied disilane offer are showed for different growth temperatures.

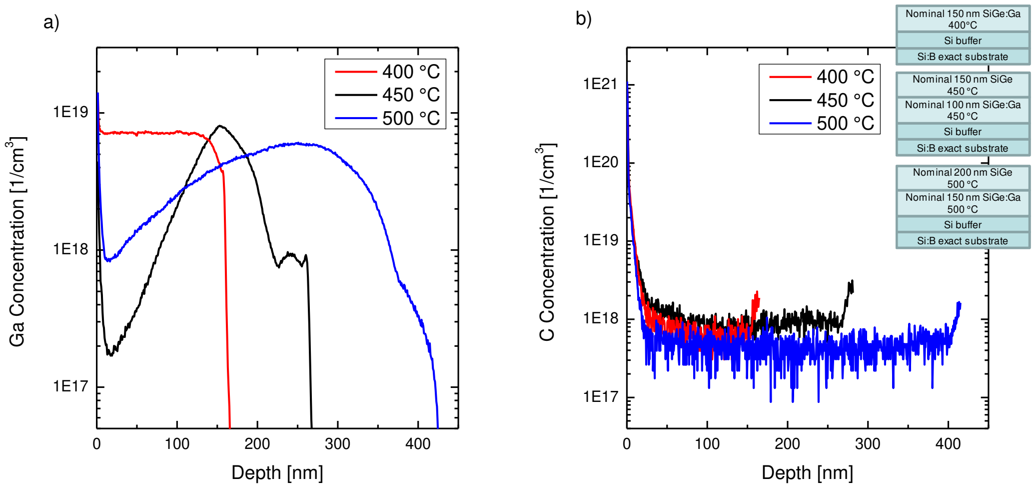

Figure 2: Ga and C SIMS profiles of SiGe samples containing around 50 % Ge grown at different temperatures. Inlet shows sample structures.

In-situ analysis of Ga(As,Bi) interfaces during low temperature growth by MOVPE

R. Günkel, T. Hepp, O. Maßmeyer and K. Volz

Department of Physics and Materials Sciences Center, Philipps-University Marburg

Various optoelectronic devices are based on a mid-infrared optical transition, such as solar cells, photodetectors and light emitters. Based on GaAs and promising a suitable transition Ga(N,As)/Ga(As,Bi) heterojunctions have type-II band alignment tunable by incorporation of the dilutes and strain. Even Ga(N,As)/Ga(As,Bi)/Ga(N,As) heterostructures so called W-type structures on GaAs (001) substrates may provide a near infrared telecom lasers[1-2].

The MOVPE growth of these structures is quite challenging. Firstly, the Ga(N,As) quantum wells (QWs) are grown at 550 °C to reduce the incorporated defects usually present during low temperature growth. Secondly the deposition of the Ga(As,Bi) QWs is conducted at 400 °C to achieve a significant Bi incorporation. Therefore, several temperature steps are needed for one sample. The challenge is to realize well-defined interfaces without grade layers or an increased interface roughness between the Ga(N,As)/Ga(As,Bi) interfaces and even enhance the Bi incorporation to reach the band gap energy for telecommunications applications. The chosen precursors are triethylgallium (TEGa) for Ga supply and tertiarybutylasane (TBAs) for As supply. To enable a smooth Ga(As,Bi) layer growth, it is necessary to cover the surface of the substrate with Bi by a preflux of trimethylbismuth (TMBi), the used Bi precursor[3]. To enhance the Bi incorporation lower growth temperature and increased growth rates are promising.

Hight resolution X-ray diffraction (HR-XRD) was used to determine the layer thickness and incorporation of dilute molar fraction related to the strain effects. The goal of the present work was an in-depth investigation of Bi incorporation behavior at 375 °C.

To investigate the interface quality during several growth experiments, reflectance anisotropy (RA) measurements on conducted as main method to get a non-destructive and instant feedback. In this type of spectroscopy, the incoming, quasi perpendicular linear polarized light is reflected from the growth interface and the difference of reflectivity of both surface directions, (-1,1,0) and (1,1,0) is normalized by their sum. Furthermore, the RA spectra are correlated to a surface reconstruction, which in turn depend on the composition and strain of fewer upper atomic layers. Those spectra can be used as fingerprints for qualitative analysis to compare or identify different surface reconstructions. In contrast, the quantitative interpretation of such measurements is an elaborate task and requires further research. By in-situ analyzing of the surface through the RA spectra, it is possible to determine the current surface reconstruction by comparing to measurements of known surfaces[4]. Quantum well growth can only be monitored by measuring the signal at a fixed energy due to the short duration of growth at the temporal resolution of the setup.

Figure 1 a) shows a Ga(As,Bi) growth series with increased TBAs supply and a fixed TEGa offer at the growth temperature of 375 °C. In addition to the incorporation of bismuth in black, the growth rate is also shown in red. It is noticeable that the growth behavior changes up to a TBAs/TEGa ratio of 1.4, which can be seen from the XRD measurements and simulations in Figure 1 b). In addition, if the TBAs/TEGa ratio is higher than 1.4, no Ga(As,Bi) growth is observed.

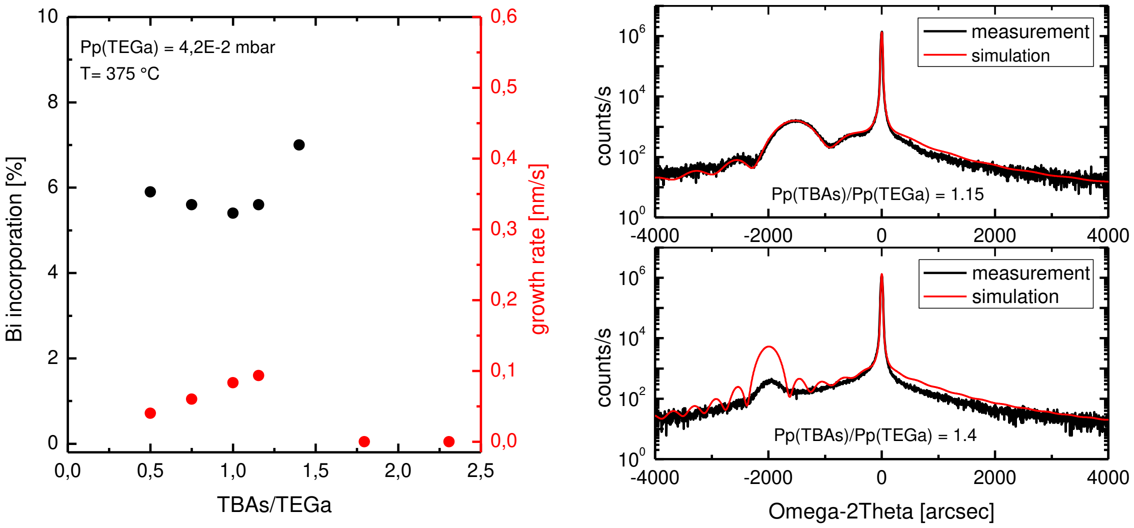

Fig. 1: a) Here the dependence of the growth rate is shown in red and that of the Bi incorporation in black on the TBAs/TEGa ratio. b) The upper HR-XRD diffractogram can be simulated well by assuming a homogeneous layer, while the lower one only shows the suitable peak position for the assumed Bi incorporation meaningfully.

Outlook

In order to understand the changed growth behavior at high TBAs supply, Ga(As,Bi) layers with tritertbutylgallium (TTBGa) can be grown, since current results show that the reaction kinetics of the TBAs decomposition can be changed by changing Ga precursors[5]. In addition, further mass spectroscopy experiments will show to what extent the different precursors for Ga(As,Bi) growth influence each other during their decomposition.

References

[1] J. Hwang and J. D. Phillips, (2011). Band structure of strain-balanced GaAsBi/GaAsN superlattices on GaAs. *Physical Review B, 83* (19), 195327.

[2] C. A. Broderick, S. Jin, I. P. Marko, K. Hild, P. Ludewig, Z. L. Bushell, W. Stolz, J. M. Rorison, E. P. O'Reilly, K. Volz, and S. J. Sweeney (2017). GaAs$_{1-x}$ Bi$_x$/GaN$_y$As$_{1-y}$ type-II quantum wells: novel strain-balanced heterostructures for GaAs-based near-and mid-infrared photonics. *Scientific reports,* 7, 46371.

[3] O. Maßmeyer, T. Hepp, R. Günkel, J. Glowatzki, W. Stolz, K. Volz (2020). In situ analysis of Bi terminated GaAs (0 0 1) and Ga(As,Bi) surfaces during growth by MOVPE. *Applied Surface Science*, *533*, 147401.

[4] P. Weightman, D. S. Martin, R. J. Cole and T. Farrell (2005). Reflection anisotropy spectroscopy. *Reports on Progress in Physics, 68* (6), 1251.

[5] O. Massmeyer, J. Haust, T. Hepp, R. Günkel, J. Glowatzki, C. von Hänisch, W. Stolz, K. Volz (2021). Revealing the Significance of Catalytic and Alkyl Exchange Reactions during GaAs and GaP Growth by MOVPE. *Submitted*

Investigation on Arsenic–Antimony- and Arsenic–Bismuth Bond Containing Interpnictogen Chain Molecules

Christian Ritter, Carsten von Hänisch*

Materials Sciences Center and Department of Chemistry, Philipps-University Marburg

Introduction

Since the DTBAA precursor for growing dilute nitride GaAs semiconductors gained high attention due to significantly better N incorporation than state of the art UDMHy, the investigation of novel group 15 compounds for possible application in MOVPE come to the fore of interests.[1,2] Therefore especially interpnictogen molecules seem to provide a lot of unexploited potential. For a focused synthesis of novel precursors a fundamental understanding on the reactivity of this class of compounds is crucial. As a result we systematically surveyed bonding situations of various pnictogen atoms in different combinations, chain lengths and attachment points of the respective group 15 elements. Earlier work on this field were undertaken by B. RINGLER in our group, who researched on chains containing a *t*Bu$_2$SbP(*t*Bu)–fragment.[3] In particular the synthesis of bonds between the heavy elements As, Sb and Bi was a key point of the current investigation, since not much information concerning their properties are given in the literature.[4–8]

Results

Conversion of *t*Bu$_2$SbCl (**I**) with *t*BuAs(H)Li·1,4-dioxane (**II**) yielded *t*Bu$_2$SbAs(H)*t*Bu (**1**) in the first place, which subsequently was lithiated to obtain the dimeric [*t*Bu$_2$SbAs(Li·thf)*t*Bu]$_2$ (**2**), since **1** showed high tendency to decompose at room temperature and under the influence of light (Scheme 1).[9] In contrast, **2** can be handled easily at room temperature and can be stored for a long period of time. In the following, **2** was used for several different reactions with the whole row of *t*Bu$_2$ECl (E = P (**III**), As (**IV**), Sb (**I**), Bi (**V**)) compounds with the intention to prepare the corresponding entirely *tert*-butyl substituted Sb–As–E-chain molecules. Unfortunately, only decomposition and formation of elemental antimony by bond cleavage of the Sb–As bond was observed. Thus, independent from the reaction conditions no products were obtained *via* this route.

Since the As–Sb bond is too weak to functionalise **1** and **2** in metathesis reactions with further pnictogens, we pursued another approach synthesising novel interpnictogen molecules with arsenic in a central position: The reaction of *t*Bu$_2$PCl (**III**) with *t*BuAs(H)Li·1,4-dioxane (**II**) selectively yielded *t*Bu$_2$PAs(H)*t*Bu (**3**) as a colourless liquid with a freezing point barely below room temperature (Scheme 1).

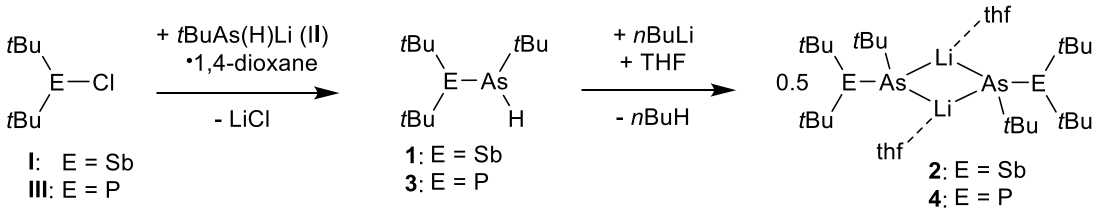

*Scheme 1: Conversion of tBu$_2$ECl (E = Sb (**I**), P (**III**)) with tBuAs(H)Li·1,4-dioxane (**II**) to tBu$_2$EAs(H)tBu (E = Sb (**1**), P (**3**)) as well as further lithiation to the dimeric [tBu$_2$SbAs(Li·thf)tBu]$_2$ (E = Sb (**2**), P (**4**)).*

In contrast to the earlier shown As–Sb bond containing compounds, **4** proves to be significantly more stable due to the stronger P–As bond. Because of the higher stability, we were now able to prepare the novel three-membered chain molecules **5–8** by conversion of **4** with **I** and **III–V**, in analogy to the work by B. RINGLER, although with different element combinations (Scheme 2). Furthermore, we were also able to obtain the four-membered chain molecules **9**–**11** by conversion of **4** with *t*Bu(Cl)E'N(H)*t*Bu (E' = P (**VI**), As (**VII**), Sb (**VIII**)) building blocks (Scheme 2). This kind of structure motive with a solely *tert*-butyl substituted pnictogen chain, especially with a remaining hydrogen atom at the nitrogen for further functionalisation, has not been known to the literature up to now.

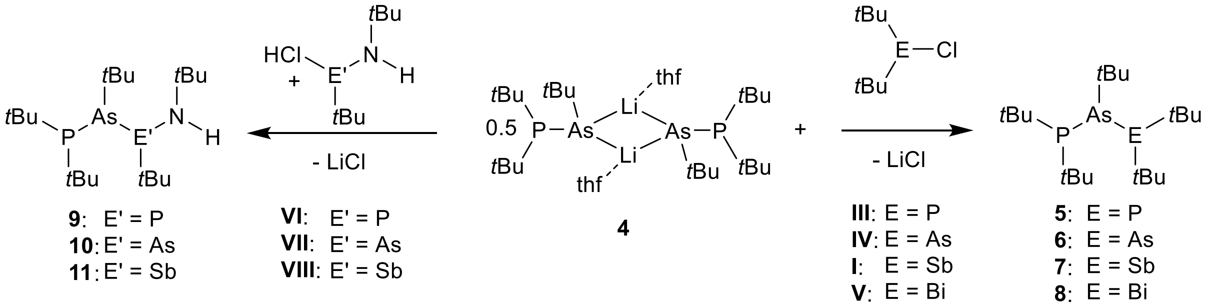

*Scheme 2: Preparation of the three-membered chain molecules **5**–**8** by conversion of **4** with **I** and **III**–**V** as well as preparation of the four-membered chain molecules **9**–**11** by conversion of **4** with **VI**–**VIII**.*

Conclusions

The targeted multistep synthesis of interpnictogen chain molecules is possible. Chain molecules with three or four different group 15 elements could be synthesised through a specific sequence of deprotonation reactions and subsequent salt metathesis. By these reactions sequences we gained insights into different bonding systems of pnictogen chains with various chain lengths and element combinations. Based on this knowledge we approached to the feasible synthesis of novel MOVPE precursors with so far unknown element combinations of the heavy homologues.

Outlook

In future works we will try to introduce the element bismuth to the four membered chains **9–11** by an initial deprotonation of the NH moiety and followed up metathesis reaction with different chlorido bismuthanes. Furthermore, we will try to transfer the obtained knowledge to the preparation of novel precursors for the MOVPE process.

References

[1] E. Sterzer, A. Beyer, L. Duschek, L. Nattermann, B. Ringler, B. Leube, A. Stegmüller, R. Tonner, C. von Hänisch, W. Stolz, K. Volz, *J. Cryst. Growth* **2016**, *439*, 19–27.
[2] E. Sterzer, B. Ringler, L. Nattermann, A. Beyer, C. von Hänisch, W. Stolz, K. Volz, *J. Cryst. Growth* **2017**, *467*, 132–136.
[3] B. Ringler, M. Müller, C. von Hänisch, *Eur. J. Inorg. Chem.* **2018**, *2018*, 640–646.
[4] N. Kuhn, M. Winter, *Chem. Ztg.* **1963**, *107*, 342.
[5] D. Nikolova, C. von Hänisch, *Eur. J. Inorg. Chem.* **2005**, *2005*, 378–382.
[6] A. J. Ashe, E. G. Ludwig, *J. Organomet. Chem.* **1986**, *303*, 197–204.
[7] K. M. Marczenko, S. S. Chitnis, *Chem. Commun.* **2020**, *56*, 8015–8018.
[8] E. Conrad, N. Burford, R. McDonald, M. J. Ferguson, *Chem. Commun.* **2010**, *46*, 4598–4600.
[9] C. Ritter, N. Michel, A. Rinow, B. Ringler, C. Hänisch, *Eur. J. Inorg. Chem.* **2021**, *2021*, 2514–2522.

Synthesis of Binary Interpnictogen Compounds from Diaryl and Dimethyl Halido Bismuthanes

Tobias Dunaj, Carsten von Hänisch

Department of Chemistry and Materials Sciences Center, Philipps-University Marburg

Introduction

Di-*tert*-butylarsane amine (DTBAA) can be used as precursor for the synthesis of 13/15-semiconductors via MOCVD methods. Using DTBAA and triethyl gallane, N-doted GaAs-semiconductors can be prepared. In comparison to the established procedure using *tert*-butyl arsane and 1,1-dimethyl hydrazine instead of DTBAA, a higher efficiency for nitrogen incorporation and a lower amount of carbon incorporation can be achieved.[1] In analogy to DTBAA, compounds with the formula $R_2Bi\text{-}PnR'_2$ (Pn = N-Sb) can be suitable as precursors for the preparation of bismuth doted semiconductors.

Only a few interpnictogen compounds incorporating the structural motif $R_2Bi\text{-}PnR'_2$ (R = Alkyl, Aryl; R' = Alkyl, Aryl, H; Pn = N, P, As, Sb) are described in the literature.[2-6] Especially for the heavier pnictogens, arsenic and antimony, compounds with covalent bonds to bismuth are very scarce, regardless of the substitution pattern on the bismuth or the lighter pnictogen atom.[6-9] By reaction of diaryl (phenyl (Ph), mesityl (Mes), 2,6-di*iso*propylphenyl (Dipp)) or dimethyl chloro bismuthanes with metalated or silylated pnictogens, we intent to prepare multiple binary interpnictogen compounds bearing, if possible, functional groups at the pnictogen atom. These binary interpnictogen compounds are tested on their usability as precursors in MOCVD processes. Moreover, further functionalization to ternary and quaternary interpnictogen compounds is attempted.

Results

Reaction of the phenyl, mesityl, as well as the Dipp substituted diaryl halido bismuthanes (Ar_2BiCl, **I-III**) with $LiNMe_2$ (**IV**) or pnictogenides of the form $LiPn^{t}Bu_2$ (Pn = P (**V**), As (**VI**)) lead to binary interpnictogen compounds with the general formula $Ar_2Bi\text{-}PnR_2$ (**1** - **3** **a** - **c**, scheme 1). Bismuthanyl stibanes (**1 h** and **3 h**) can be accessed *via* reaction of the bismuthane amines **1 a** or **3 a** and Mes_2SbH (**VII**, scheme 1). Reaction of the **2 a** and **3 a** with *tert*-butyl amine yielded functional bismuthane amines through elimination of dimethylamine (**2 e**, **3 e**, scheme 1).

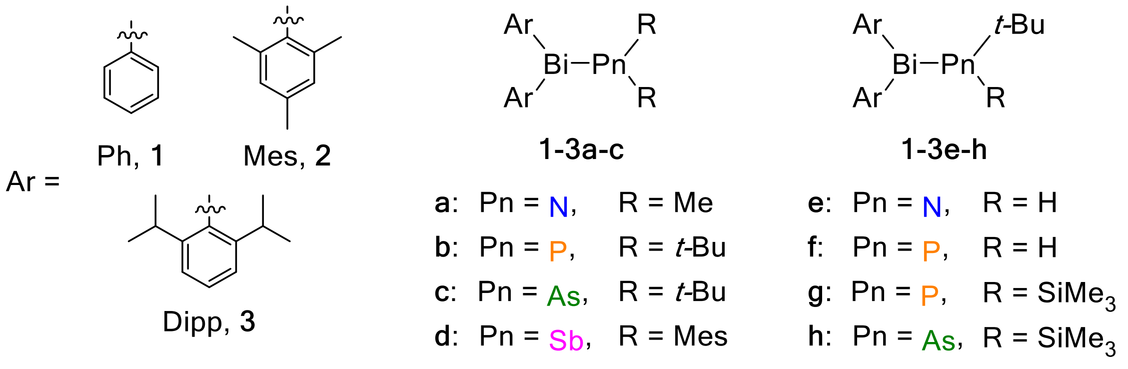

Scheme 1: Prepared diaryl bismuthanyl pnictogens.

Using the synthetic route of trimethylsilyl halide elimination instead of salt metathesis, a bismuthanyl phosphane with a proton at the phosphorus center was isolated (**3 f**, scheme 1). Moreover, multiple bismuthanyl phosphanes and arsanes bearing trimethylsilyl substituents were obtained (**1** - **3** **g** - **h**, scheme 1).

A major problem of all diaryl bismuthanyl pnictogens regarding the application in the MOCVD process is the relatively low vapour pressure of these solid compounds. In order to obtain liquid compounds with a higher vapour pressure, we exchanged the two aryl substituents through methyl substituents. By reaction of Me_2BiCl (**VIII**) with **V** or **VI**, the liquid $Me_2BiP\textit{t}Bu_2$ (**4**) and $Me_2BiAs\textit{t}Bu_2$ (**5**) are obtained. Due to thermal lability of these compounds, with fast decomposition starting at around 65 °C, the preparation of larger quantities of **4** and **5** remains challenging.

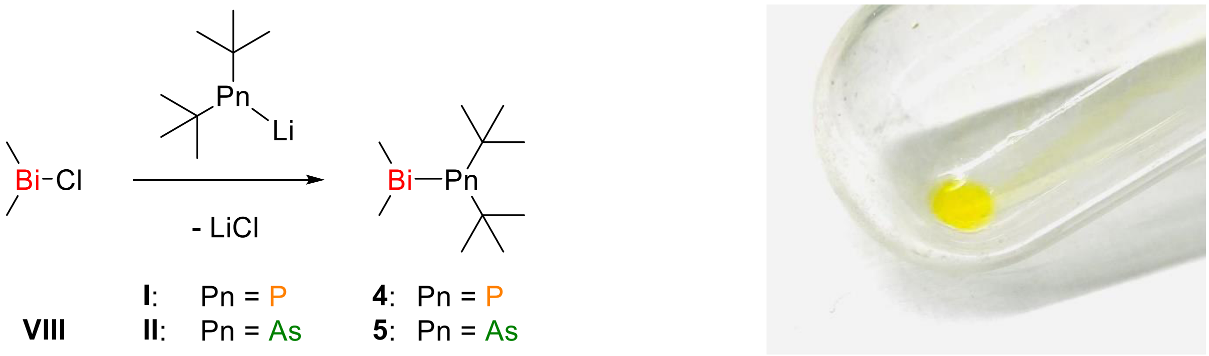

*Scheme 2: left: Preparation a liquid, dimethyl bismuthanyl phosphane (**4**) and arsane (**5**). right: picture of 0.2 ml of the liquid compound **5**.*

Conclusion and Outlook

Many binary diaryl bismuthanyl pnictogens, some of which bear functional groups, have been successfully prepared. Additionally, liquid binary interpnictogen compounds bearing methyl substituents at the bismuth center were synthesized. These compounds might be suitable precursors for application in the MOCVD processes.

In future experiments we want to optimize the preparation and purification of compounds **4** and **5**. Additionally, we plan to prepare bismuthanyl phosphanes and arsanes with smaller substituents to further enhance the volatility of the binary interpnictogen compounds. Moreover, we want to prepare liquid bismuthaneamines which will hopefully show higher thermally stability than their heavier homologues. This would allow easier workup and storage of the potential precursors.

References

[1] C. von Hänisch, W. Stolz, K. Volz, *J. Cryst. Growth* **2016**, *439*, 19–27.
[2] A. J. Ashe III, E. G. Ludwig Jr., *J. Organomet. Chem.* **1986**, *303*, 197–204.
[3] H. J. Breunig, D. Müller, *Z. Naturforsch. B* **1986**, *41B*, 1129–1132.
[4] R. J. Schwamm, M. Lein, M. P. Coles, C. M. Fitchett, *Angew. Chem.* **2016**, *55*, 14798–14801.
[5] C. Ritter, B. Ringler, F. Dankert, M. Conrad, F. Kraus, C. von Hänisch, *Dalton Trans.* **2019**, *48*, 5253–5262.
[6] S. Traut, A. P. Hähnel, C. von Hänisch, *Dalton Trans.* **2011**, *40*, 1365-1371.
[7] C. Ritter, N. Michel, A. Rinow, B. Ringler, C. von Hänisch *Eur. J. Inorg. Chem.* **2021**, *25*, 2514–2522.
[8] K. M. Marczenkoa, S. S. Chitnis, *Chem. Commun.*, **2020**, *56*, 8015–8018.
[9] L. Dütsch, C. Riesinger, G. Balázs, M. Scheer, *Chem. Eur. J.*, **2021**, *27*, 8804–8810.

The influence of excitation power and temperature on the luminescence properties and offset of Ga(As,Sb)-based type II heterostructures

Luise Rost, Jannik Lehr, Wolfgang Stolz and Wolfram Heimbrodt

Department of Physics and Materials Sciences Center, Philipps-University Marburg

Introduction

Infra-red semiconductor lasers for long-range optical communication using optical fibers are still a highly topical field. There are many ways to achieve long wavelength lasing in the range of 1.3 µm.

A strategy to get to longer wavelength and to overcome Auger losses is the use of type-II devices, where the recombining electrons and holes are spatially separated [1,2]. Additionally, such systems offer more degrees of freedom for device design as the band edges of the electron and the hole confining wells can be varied independently allowing for a wide tuning of the type-II transition energy. A promising heterostructure design for such applications are so called W-laser structures which enable the optimization of the wave function overlap by adding barrier layers to confine carriers. With the continuing progress of device miniaturization in mind, the properties of the internal interfaces are getting more and more important. In this study, we present as thorough investigation of photoluminescence properties of (Ga,In)As/GaAs/Ga(As,Sb) heterostructures with modified interface morphology.

Results

In a previous paper we could show that one can improve the type-II photoluminescence efficiency by smoothening the interface of (Ga,In)As [3]. As extremely sensitive probe the type-II recombination has been used of (Ga,In)As/GaAs/Ga(As,Sb) double quantum well (DQW) heterostructures. By applying a 120 s growth interruption (GI) after growth of the (Ga,In)As layer and prior to the growth of the next layer a smoothening of the interface and enhanced luminescence efficiency was found. A detailed analysis of the other relevant layer Ga(As,Sb) and its relevance for a high quantum efficiency of the W-laser was missing so far.

We used the inverted DQW Ga(As,Sb)/GaAs/(Ga,In)As to analyze the influence of GI on the morphology of Ga(As,Sb) layers and the luminescence properties, particularly the recombination dynamics of the charge transfer (CT) recombination processes. We were able to reveal the strong correlation of the type-II luminescence intensity and lifetime with the morphology of the Ga(As,Sb) layer and interfaces [4].

With the new-found growth conditions for both relevant layers we want to dive deeper into the understanding of the type-II recombination and the specifics of the material system. So, we had a look which influence the excitation power and the temperature have on the offset between the two materials. In Figure 1 you can see, that with enough laser power you can nearly suppress the type-II recombination. This is due to low conduction band offset between (Ga,In)As und Ga(As,Sb). The type-I transition of the Ga(As,Sb) doesn't shift in energy but the peak clearly broadens.

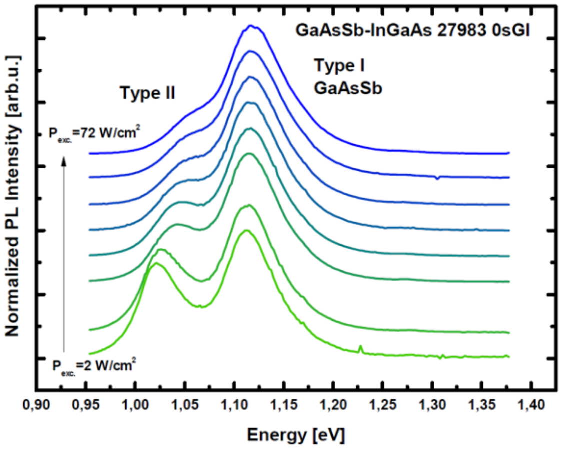

Fig. 1: Photoluminescence at room temperature with varied excitation power.

Another interesting thing is the temperature depended behaviour of the offset. Due to the nature of the type-II transition, you can calculate the offset if you have the energy of both type-I transitions and the type-II transition. For the temperature dependence we varied the temperature from 100 K to 250 K and detected all necessary transitions to calculate the offset.

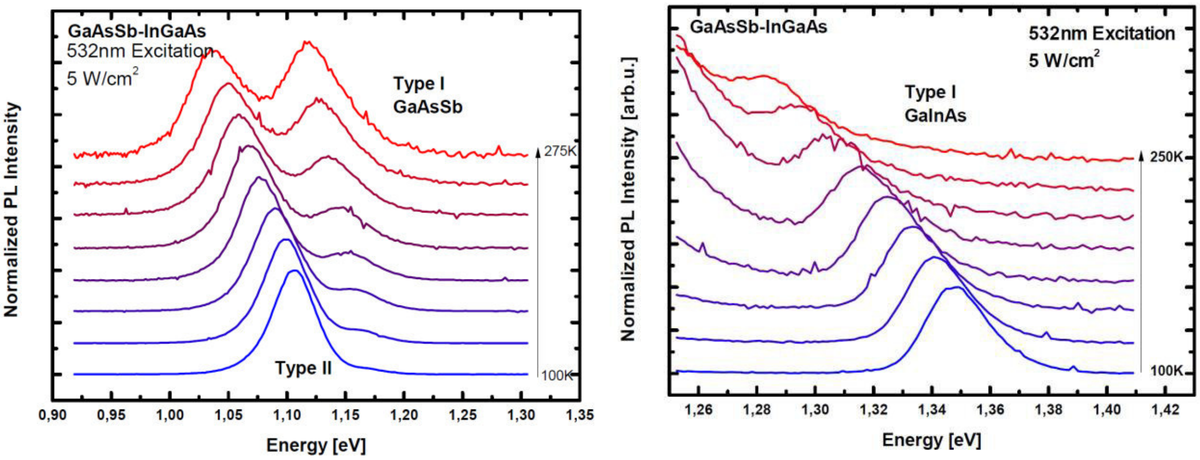

Fig. 2: Spectra of the Photoluminescence with varied temperature. The spectra shifted do to better visualization.

Outlook

We like to further investigate the recombination dynamics of charge transfer processes at 10 K, for that we had the opportunity to measure with a streak camera at group from Prof. Chatterjee at JLU Gießen. There we would like to also resonantly excite separately the two different quantum wells and have a look of the temporal evolution of the type-II transition. Furthermore, I will finish my thesis.

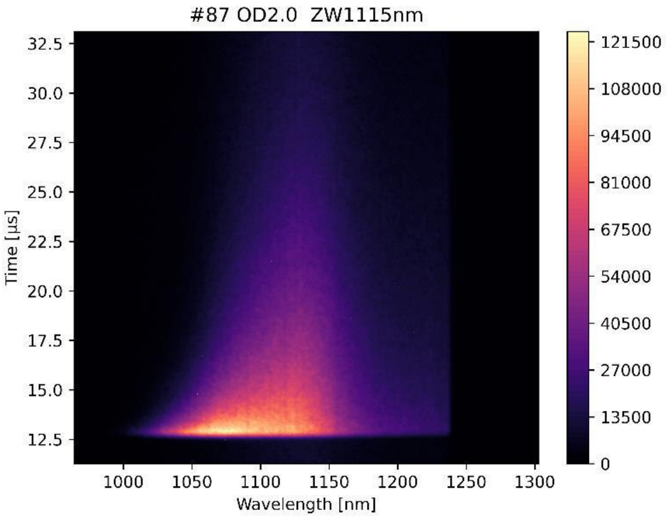

Fig. 3: Image from the streak camera measurement for the sample 27987.

References

[1] C. Berger, C. Möller, P. Hens, C. Fuchs, W. Stolz, S. W. Koch, A. Ruiz Perez, J. Hader, and J. V. Moloney, AIP Adv. **5**, 047105 (2015).

[2] S. Gies, C. Kruska, C. Berger, P. Hens, C. Fuchs, A. Ruiz Perez, N. W. Rosemann, J. Veletas, S. Chatterjee, W. Stolz, S. W. Koch, J. Hader, J. V. Moloney, and W. Heimbrodt, Appl. Phys. Lett. **107**, 182104 (2015).

[3] L. Rost, S. Gies, M. Stein, C. Fuchs, S. Nau, P. Kükelhan, K. Volz, W. Stolz, M. Koch, and W. Heimbrodt, J. Phys. Condens. Matter **31**, 014001 (2019).

[4] L. Rost, J. Lehr, M. Maradiya, L. Hellweg, F. Fillsack, W. Stolz, W. Heimbrodt, J. Luminescence **231**, 117817 (2021).

In-situ TEM Investigations of III/V Semiconductor Materials

Maximilian Widemann, David Krug, Felix Gruber, Andreas Beyer, Kerstin Volz

Materials Sciences Center and Department of Physics, Philipps-University Marburg

Introduction

III/V semiconductors are used for many technical applications, like for example LEDs, lasers and solar cells. A widely used fabrication process of these materials is metal organic vapor phase epitaxy (MOVPE). However, structural investigations of the samples are usually carried out post growth. *In-situ* studies of the growth process promise an improvement of the fabricated materials performance. But it comes along with several challenges, like the realization of the growth conditions inside a TEM or the incongruent evaporation of the group V compound at elevated temperatures. *In-situ* (scanning) transmission electron microscopy ((S)TEM) allows to investigate dynamic processes, which occur during the thermal annealing or the growth of III/V semiconductor materials inside a TEM. Gas environmental cell and heating holders enable to supply gases while heating the sample, so that conditions comparable to those during the MOVPE process can be realized in any electron microscope[1].

Methods

To this end, a commercially available Protochips *in-situ* system has been modified. In order to allow the usage of toxic and pyrophoric gases, like the precursor gases used in MOVPE growth a gas mixing system, an appropriate gas monitoring system as well as a gas scrubbing system have been added to the setup[2]. To analyze the compounds of the gases and to detect reaction products a SRS 200 amu residual gas analyzer (RGA) has been integrated. A sample preparation technique is necessary, which allows a controlled transfer of a microscopic and electron transparent sample onto a micro electro mechanical system (MEMS) chip of gas environmental cell holder[3]. This is given by the focused ion beam (FIB) lift out technique and is performed in a JEOL JIB-4601F dual beam system. A double C_S-corrected JEOL JEM 2200FS operating at 200 kV is used for the TEM observations. As a model system GaP nanowires (NW) have been investigated in first growth experiments, since their growth observation comes along with less challenges compared to layer growth processes. Precursor gases used for GaP based experiments are tertiarybutylphosphine (TBP) and trimethylgallium (TMGa). Additionally, N_2 can be used as carrier gas.

Obviously, there is a huge geometrical difference between macroscopic bulk samples and microscopic TEM samples, which have a much higher surface to volume ratio. Nevertheless, thermal stability of these samples under elevated temperatures, which are required for annealing or crystal growth, can be achieved like it is done for bulk samples by a surplus of the group V precursor gas[2]. Furthermore, the microscopic geometry of the closed cell holder, which acts as MOVPE reactor, is capable of decomposing the precursor gases and grow crystalline materials from gas phase.

NW vapor liquid solid (VLS) growth experiments catalyzed by gold nanoparticles (NP) have been performed with a total pressure of 400 hPa and precursor partial pressures between 10^{-1} hPa and 10^{-3} hPa with a V/III ratio of 10. Growth temperature has been varied between 400 °C and 450 °C.

To prove the comparability of the TEM holder reactor to a commercial MOVPE machine, the thermal decomposition of TBP is investigated.

Results

The experiments demonstrate the influence of the growth parameters on the NW morphology and growth rate. Temperature strongly determines the shape of the NWs. At 450 °C grown samples show a straight growth behavior, whereas NWs grown at 400 °C form many kinks. Measurements of these kinking angles show a predominance of 70° (Fig. 1 a). This is most probably caused by twin boundaries (Fig. 2 b)[4]. This defect appears on the gallium terminated (111) surfaces[5]. The reason why the 70° angle is formed more often than the 110° angle, which might be caused by this defect as well, may be given by the conservation of the layer formation order, which is assumed to be from gallium to phosphorus. A further frequently observed angle is around 123°. These angles can occur when twins of second order are formed, meaning two twins after another.

The growth rate of the NWs can be controlled mainly by the partial pressures of the precursor gases. Higher partial pressures lead to an increased incorporation of growth material. Another crucial factor for the growth rate is given by the surface ratio of droplet and growth plane. NWs with different surface ratios can be seen in the STEM images in Fig. 2 a during the growth at 450 °C and partial pressures of 1.6×10^{-2} hPa (TBP) and 1.8×10^{-3} hPa (TMGa). The wires show a big difference in the surface ratios, resulting in growth rates of 39.9 nm/s and 2.7 nm/s under the same conditions respectively. Since the incorporated material needs to diffuse across the droplet surface through the liquid catalyst, a higher droplet surface leads to more diffusion of the limiting species growth material. Whereas an increased interface area between droplet and growth plane reduces the growth rate. Fig. 2 b show the growth rate for 13 different NWs of this experiment in dependence of their surface ratios, indicating a linear proportionality.

Furthermore, we compare the growth of nanowires in post growth investigations with applying the same growth conditions with and without electron beam, respectively. All in all, the electron beam seems to have a negligible influence on nanowire growth under appropriate conditions. This suggests that results, collected in *in-situ* TEM growth investigations, can be transferred to processes appearing in conventional MOVPE growth.

These observations are supported by the results of the thermal decomposition behavior of precursor gases at the example of TBP. Figure 3 shows the decomposition signal of TBP in dependence of temperature. The green curve displays the mass spectrometry signal of the undecomposed molecule. The decomposition starts at a temperature of around 650 °C, at which the signal begins to drop and the signal of the formed phosphine (red curve) rises. At a temperature of 950 °C only 33 % of the TBP molecules are decomposed. The tiny reactor volume and heated surface lead to less efficient pyrolysis compared to conventional MOVPE reactors. The signals generated by the produced isobutane (orange curves) and isobutene (blue curves) give insights to the decomposition pathways of TBP. Isobutane is formed due to homolytic fission, whereas isobutene is generated in β-hydrogen elimination. One can see that with rising temperature the formation of isobutene is increased and less isobutane is generated. Hence β-hydrogen elimination becomes more and homolytic fission less favorable. This is consistent with findings in decomposition studies of TBP[6], indication the comparability of the micrometer scale reactor to conventional reactors.

Outlook

In further *in-situ* growth experiments, the detailed dependencies of temperature and precursor partial pressures as well as the catalyst droplet geometry on the growth rate needs to be investigated. Also images and videos of atomic resolved layer formation are still missing. To achieve this, a sample preparation technique is needed to prepare NWs on a substrate, which determines the crystal orientation. Since the closed gas cell holder has only single tilt capabilities, it is only reliable to tilt NWs into zone axis with control over the crystal orientation. Additionally, atomic resolved images of twin boundaries causing the 70° kinking angles are to come. Moreover, the insights gained in *in-situ* TEM growth investigations need to be transferred to growth mechanisms like they appear in the MOVPE layer growth. Such experiments require substrate samples in zone axis, which can be achieved by the FIB lift out technique. A further important question which needs to be clarified is the influence of the electron beam on the sample as well as on the gas phase. To this end residual gas analysis of precursors irradiated with the electron beam will be compared to the ones presented above. This promises a deeper understanding of the processes taking place in a MOVPE growth machine, leading to the improvement of grown materials properties.

References

[1] Lawrence F. Allard et al. "A new MEMS-based system for ultra-high-resolution imaging at elevated temperatures." *Microscopy Research and Technique* 72.3 (2009): 208-215.

[2] Rainer Straubinger et al. "In Situ Thermal Annealing Transmission Electron Microscopy (TEM) Investigation of III/V Semiconductor Heterostructures Using a Setup for Safe Usage of Toxic and Pyrophoric Gases." *Microscopy and Microanalysis* 23.4 (2017): 751-757.

[3] Rainer Straubinger, Andreas Beyer, and Kerstin Volz. "Preparation and loading process of single crystalline samples into a gas environmental cell holder for in situ atomic resolution scanning transmission electron microscopic observation." *Microscopy and Microanalysis* 22.3 (2016): 515-519.

[4] Minghuan Zhang et al. "Formation mechanisms for the dominant kinks with different angles in InP nanowires." *Nanoscale Research Letters* 9.1 (2014): 211.

[5] Andreas Beyer et al. "Influence of crystal polarity on crystal defects in GaP grown on exact Si (001)." *Journal of Applied Physics* 109.8 (2011): 083529.

[6] S. H. Li et al. "Pyrolysis of tertiarybutylphosphine." *Journal of Electronic Materials* 18.3 (1989): 457-464.

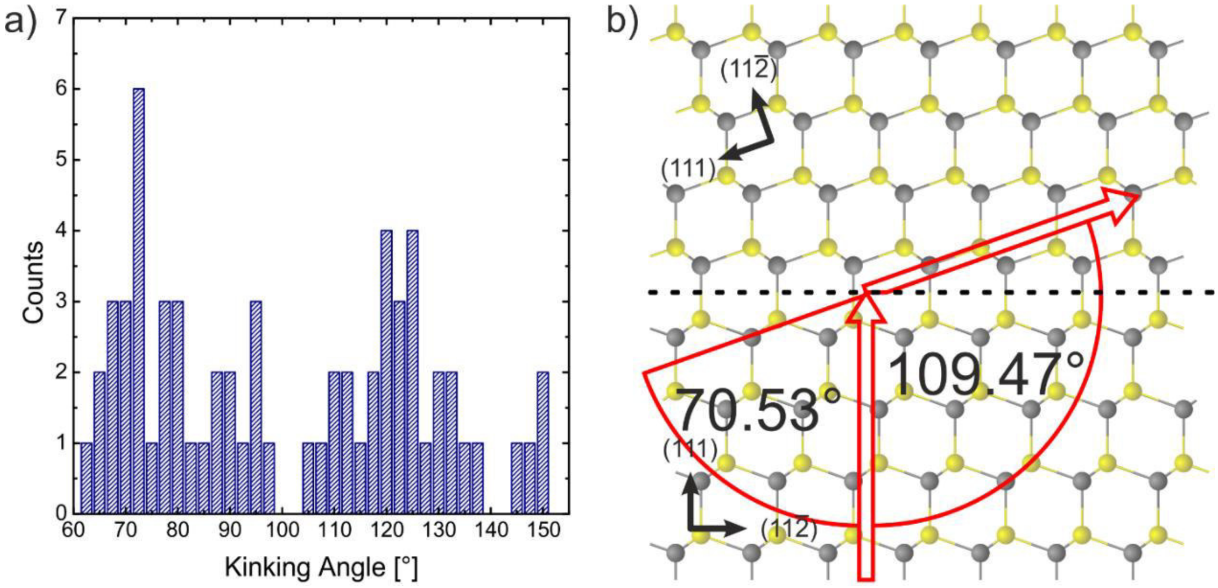

Fig. 1: a) Histogram of kinking angles of NWs grown at 400 °C. The predominance of 70°, 110° and 123° indicates twin boundary defects causing these kinks. b) Schematic drawing of a twin boundary (black line) in $[1\bar{1}\,0]$ projection.

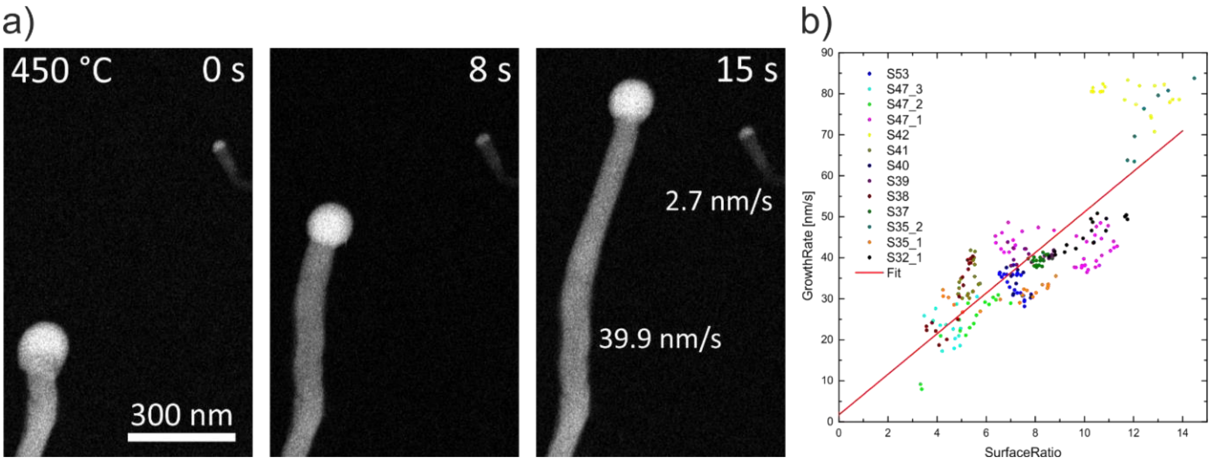

Fig. 2: a) STEM images of two growing NWs. The deviating surface ratios lead to different growth rates. b) Growth rate measurements of 13 NWs in dependence of their surface ratio. Each color represents a single NW.

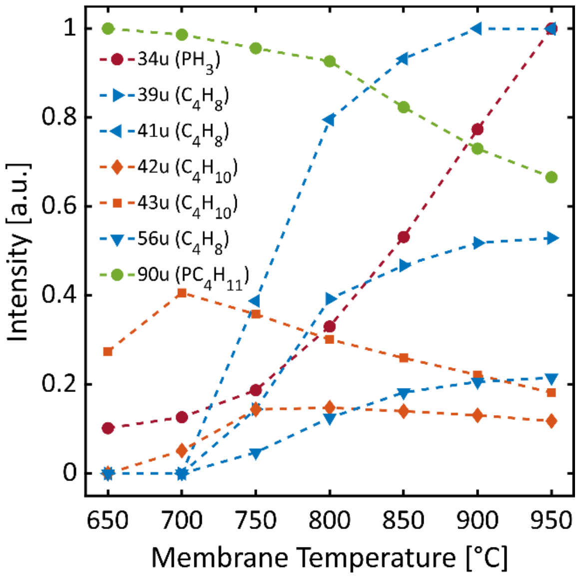

Fig. 3: Decomposition products of TBP versus temperature. The decrease of TBP can be seen (green), while the phosphine intensity rises (red). Isobutene (blue) formation becomes more favorable with temperature, whereas isobutane (orange) formation is reduced.

Optoelectronic Coupling between Colloidal Quantum Dots and Semiconductor Substrates

Mikko Wilhelm, Ebru Kartal and Wolfram Heimbrodt

Department of Physics, Philipps-University Marburg

Introduction

The optoelectronic interaction between colloidal II-VI semiconductor quantum dots (QDs) and different semiconductor substrates is studied. The colloidal quantum dots provide a simple and low-cost way to functionalize the semiconductor substrates with a variety of physical properties by modifying the size, shape, and composition of the quantum dots. Such hybrids are promising systems for applications as gas sensors, photo sensors or solar cells.

In this work CdS/ZnS and CdSe/ZnS core shell quantum dots are transferred from solution via knife coating to the substrates to create a thin layer of quantum dots linked via Van der Waals interaction to the substrate. Different substrates like ZnSe, ZnMnSe, GaP, TiO_2, ZnO and quartz are used. The aim is to investigate and describe the interaction between the QDs and semiconductor substrates, especially regarding energy and charge transfer in these hybrid structures.

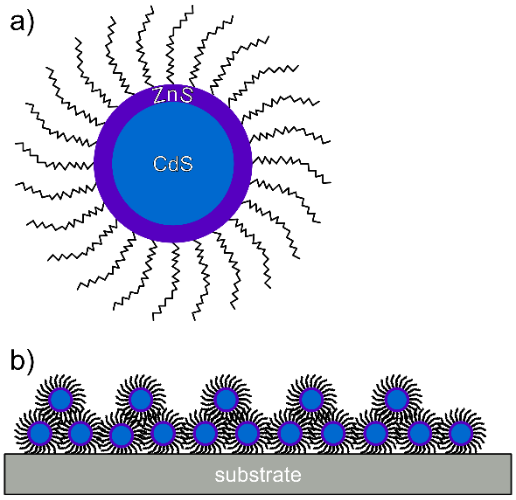

Fig. 1: Schematic representation of the quantum dots and aa dried layer on the semiconductor substrate.

Results

The hybrid structures were characterized by continuous-wave and nanosecond time-resolved photoluminescence measurements at different temperatures. The dominant transfer processes between the QDs and the substrate depend on the distance and the band alignment in the coupled structures. It is well known that the band gap E^{QD} of the QDs is dependent on their radius R and the effective masses of the electron and hole m^* according to the Brus equation:

$$E^{QD} = E_{gap} + \frac{h^2}{8\,R^2}\left(\frac{1}{m_e^*} + \frac{1}{m_h^*}\right) - \frac{1.8\,e^2}{4\,\pi\,\varepsilon_0\varepsilon_r R}$$

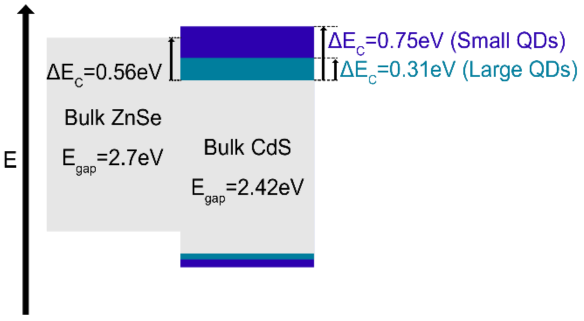

Fig. 2 Estimated band alignment between the quantum dots and the substrate at T=290K.

Thus, it is possible to tune the band alignment and with it the transfer processes in the hybrid structures by using quantum dots of different sizes. The effect of the size on the band alignment for the CdS/ZnS quantum dots on a ZnSe substrate is shown in Figure 2. Energy transfer from the quantum dots should be possible if their band gap is larger than the band gap of the substrate. Electron transfer can happen from the higher energy band to the lower band. In all cases, only the quantum dots close to the interface participate in the transfer processes. That is why it is important to create thin layers of quantum dots. Absorption measurements of prepared quantum dots on quartz indicate a layer thickness of only very few monolayers. The transfer process can be investigated with the decay curves of the respective photoluminescence bands, as shown in Figure 3. Quantum dots on quartz are taken as a reference. The PL is observable for hundreds of nanoseconds after excitation. Additional transfer processes lead to a faster PL decay.

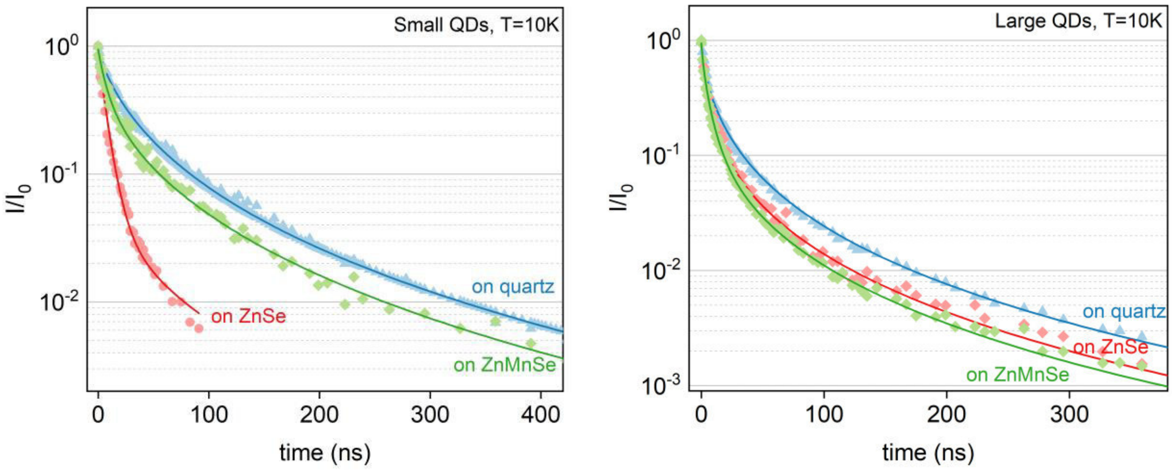

Fig. 3: Photoluminescence decay curves of the small QDs (left) and large QDs (right) on different substrates. The curves are fitted according to equation (2).

To quantitively describe the PL decay the curves can be fitted with the following equation, assuming a distribution of decay times $\rho(\tau')$, an average transfer time τ_{trf} and triplet feeding time τ_{trip}:

$$I(t) = \left(1 - c + c\exp\left(\frac{-t}{\tau_{trf}}\right)\right) A_0 \int_0^{\infty} \rho(\tau')\exp\left(\frac{-t}{\tau'}\right) d\tau' + (1-c)\, B_0\ \exp\left(\frac{-t}{\tau_{trip}}\right)$$

The kind of transfer processes is then determined comparing different hybrid structures with different band alignments. A strong transfer can be observed for high energy quantum dots on ZnSe, this transfer is impaired when the ZnSe is doped with manganese or when lower energy quantum dots are used.

Similar transfer processes are observed for CdSe/ZnS quantum dots (instead of CdS/ZnS) on different substrates, as shown in Figure 3. The PL decays faster on materials with a smaller bandgap, likely due to energy transfer processes.

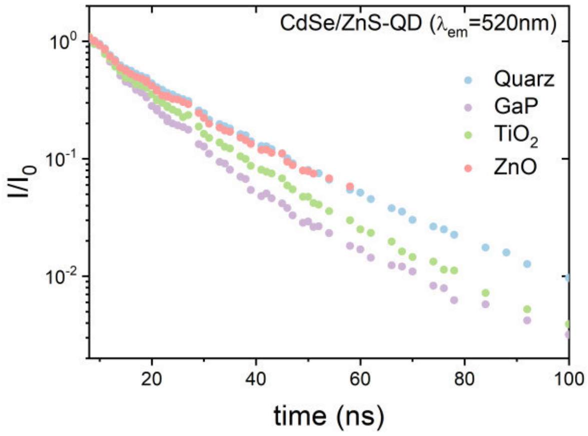

Fig. 4: Photoluminescence decay curves of CdSe/ZnS QDs on different substrates.

Conclusion

The energy and charge transfer processes in hybrid structures consisting of core shell CDs and semiconductor substrates was studied. It was possible to prepare these hybrid structures with a thin layer of quantum dots by using a simple and low-cost method. A transfer from the quantum dots to suitable substrate could be observed. The transfer mechanism is changed by using quantum dots of different sizes or by changing the substrate. The different band alignment of quantum dots and substrates studied to help differentiate between the possible transfer processes.

Theoretical investigation of azulene and naphthalene on Si(001)

Florian Kreuter, Ralf Tonner

Wilhelm-Ostwald-Institute for Physical and Theoretical Chemistry,
Faculty of Chemistry and Mineralogy, University Leipzig

Introduction

In material science, the Si(001) surface is one of the most investigated surfaces due to its interesting electronic properties. The surface is ideal for organic functionalization for its high reactivity caused by the buckled-dimer reconstruction.[1] The upper $\mathrm{Si_{up}}$ dimer atom is nucleophile, whereas the other $\mathrm{Si_{down}}$ dimer atom is electrophile.[2] Therefore, many studies investigated the adsorption of organic molecules on Si(001).[3] In our group, the adsorption of organic adsorbates on Si(001) has been extensively investigated.[4]

One interesting organic molecule is azulene due to its unusually large dipole moment. The adsorption of azulene has been computationally extensively investigated on metallic surface in collaboration with the experimental studies conducted in the Gottfried group.[5] These studies show that the interaction between azulene and metal surfaces is particularly strong due to its non-alternating aromatic structure. But up to now, it remains open if azulene also shows unusual reactivity on Si(001) - neither experimental nor computational studies are available.

This study therefore aims to investigate the adsorption of azulene on Si(001). In addition, the alternating-aromatic isomer naphthalene will be investigated. The influence of aromaticity on the adsorption can be studied by comparing the results of azulene and naphthalene on Si(001).

Methods

All investigations are carried out applying density functional theory (DFT). First, the optimized structure of both molecules on the surface is determined. To this end, different starting structures need to be generated and optimized with the program package VASP.[6] The bonding energy of different structures is compared. In addition to the structures hand-picked by “chemical intuition”, an optimization scheme by ab initio molecular dynamic simulations (AIMD) will be used to check that interesting structures are not overlooked. In AIMD, thermally excited movement of the molecules on Si(001) surface is simulated. If the simulation is long enough, the molecule should run through all possible conformers of the adsorption product. Several trajectories will be run on a supercomputer to ensure that different adsorption paths are found.

The adsorption paths are calculated by using the nudged elastic band with Climbing Images (NEB-CI) method.[7] The optimized molecules are set 9 Å over surface as the starting structure for the path, and the chemisorbed structures were the final structure of the path. Additionally, the path from the physisorbed state into the chemisorbed state is computed for naphthalene.

Finally, the character of the molecule-surface bond will be analyzed. To this end, the energy decomposition analysis for extended systems (pEDA)[8] is used by ADF program package. In pEDA, the bonding energy is divided into several physically well-defined terms, which make it easier to interpret the bonding character. Also, the system is split into fragments that interact for building the bonds. The first term is the preparation energy. This term describes the energy that is needed for deforming the fragments from their ground state structure to the structure in the system. Further pEDA terms are the electrostatic contribution (quasiclassical electrostatic interaction between densities of the two fragments), Pauli repulsion and orbital contribution.

An additional term that is highly relevant for surface adsorption is dispersion interaction which is not captured by standard density functionals. In this project, the DFT-D3 method by Grimme et al. is applied to derive the dispersion energies.[9]

Results

Both azulene and naphthalene interact strongly with Si(001). The interaction is stronger for azulene (E_{ads} = -289 kJ/mol) than for naphthalene (-267 kJ/mol). This corresponds to the results on the metal surface.[5] The chemisorption on Si(001) is also confirmed by pEDA results. These show that four covalent C-Si bonds are formed in both cases. The exact character of the bonds of two molecules on the surface can't be determined, since the description as donor-acceptor and as electron share bonding give similar results. Furthermore, a surface-to-molecule can be seen from the pEDA calculations, which is confirmed by partial charge analysis. Several different chemisorbed states are found for azulene, with 4 or 3 C-Si bonds. In the best structure, 3 C atoms from the 7-ring and an atom from the 5-ring are bonded, with the molecule rotated by 50° to the Si dimer row. In contrast, for naphthalene, only 2 chemisorbed states (parallel and perpendicular to Si dimer row) with C1, C4, C5, C8 atoms bonded were found, and several physisorbed states. The perpendicular one is more stable.

In addition to the structure and the binding analysis, the adsorption paths were investigated. Both AIMD and NEB calculations show a direct absorption path for azulene. The absorption path for naphthalene isn't directly from vacuum or a physisorbed state. In both, a precursor occurs with only one ring bonded. The activation energy from these precursors into the final structure is very small (about 6 kJ/mol). Therefore, this adsorption path can be labeled as pseudo direct. Naphthalene probably has a narrow adsorption funnel. This is because it was very difficult for naphthalene to find the chemisorbed structures by optimization and AIMD.

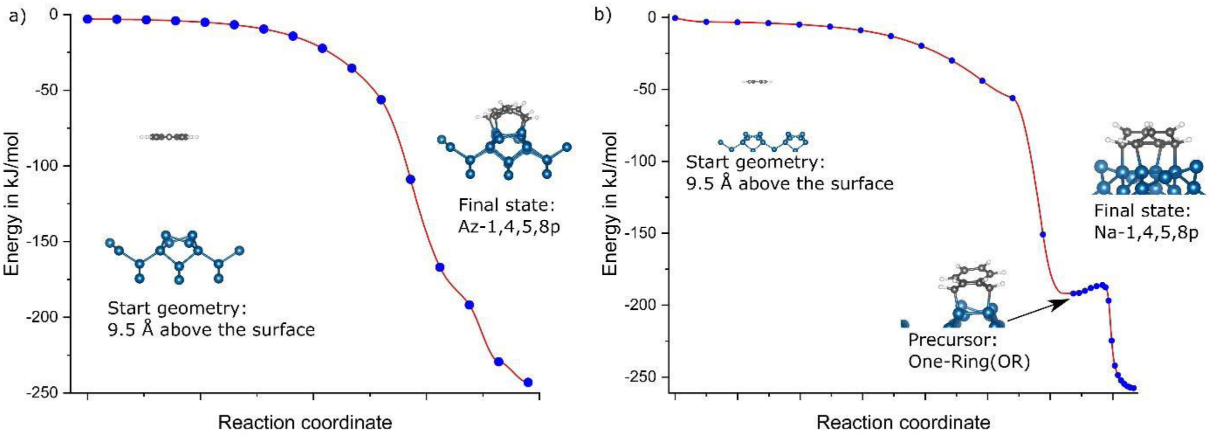

Figure 1: Adsorption path for azulene (a) and naphthalene (b) from vacuum to Si(001)

Outlook

The results obtained should perhaps inspire experimental studies due to the interesting found properties of azulene on Si(001) surfaces such as the direct adsorption path. From a theoretical point of view, plans for this topic are to investigate the adsorption paths for naphthalene in more detail. For this purpose, a method is to be used, which scans the space and determines the absorption path of the different space points. The goal is to find all pathways and to understand how narrow the funnel is for the pseudo-direct adsorption path.

References

[1] R. E. Schlier, H. E. Farnsworth, *J. Chem. Phys.* **1959**, *30*, 917.

[2] J. Yoshinobu, *Progress in Surface Science* **2004**, *77*, 37.

[3] A. V. Teplyakov, S. F. Bent, *Journal of Vacuum Science & Technology A* **2013**, *31*, 50810.

[4] a) L. Pecher, G. Mette, M. Dürr, R. Tonner, *ChemPhysChem* **2017**, *18*, 357;
b) L. Pecher, R. Tonner, *ChemPhysChem* **2017**, *18*, 34;
c) L. Pecher, S. Laref, M. Raupach, R. Tonner, *Angew. Chem. Int. Ed.* **2017**, *56*, 15150;
d) L. Pecher, S. Schmidt, R. Tonner, *J. Phys. Chem. C* **2017**, *121*, 26840;
e) L. Pecher, C. Schober, R. Tonner, *Chem. Eur. J.* **2017**, *23*, 5459.

[5] a) S. R. Kachel, B. P. Klein, J. M. Morbec et al., *J. Phys. Chem. C* **2020**, *124*, 8257;
b) B. P. Klein, S. E. Harman, L. Ruppenthal et al., *Chem. Mater.* **2020**, *32*, 1041;
c) B. P. Klein, J. M. Morbec, M. Franke et al., *J. Phys. Chem. C* **2019**, *123*, 29219;
d) B. P. Klein, N. J. van der Heijden, S. R. Kachel et al., *Phys. Rev. X* **2019**, *9*, 011030

[6] a) G. Kresse, J. Hafner, *Phys. Rev. B* **1993**, *47*, 558;
b) G. Kresse, J. Hafner, *Phys. Rev. B* **1994**, *49*, 14251;
c) G. Kresse, J. Furthmüller, *Phys. Rev. B* **1996**, *54*, 11169;
d) G. Kresse, J. Furthmüller, *Comput. Mater. Sci.* **1996**, *6*, 15-50.

[7] a) G. Henkelman, B. P. Uberuaga, H. Jónsson, *J. Chem. Phys.* **2000**, *113*, 9901;
b) G. Henkelman, H. Jónsson, *J. Chem. Phys.* **2000**, *113*, 9978;
c) H. Jónsson, G. Mills, K. W. Jacobsen in *Classical and Quantum Dynamics in Condensed Phase Simulations* (Eds.: B. J. Berne, G. Ciccotti, D. F. Coker), World Scientific, **1998**, 385-404.

[8] M. Raupach, R. Tonner, *J. Chem. Phys.* **2015**, *142*, 194105.

[9] a) S. Grimme, J. Antony, S. Ehrlich, H. Krieg, *J. Chem. Phys.* **2010**, *132*, 154104;
b) S. Grimme, S. Ehrlich, L. Goerigk, *J. Comput. Chem.* **2011**, *32*, 1456.

Strain induced direct-indirect transition in ternary III-V semiconductor from ab-initio approach

Badal Mondal, Ralf Tonner

Wilhelm-Ostwald-Institute for Physical and Theoretical Chemistry
University Leipzig, 04103 Leipzig, Germany

Introduction

Investigations on effect of strain on the electronic properties of ternary III/V semiconductors have remained scientifically demanding and an exciting field for the last few decades by the name 'strain engineering' in semiconductor. Observations from our previous strain study on binary III-V semiconductor led to our primary focus for this new project on one of the most interesting phenomena: direct-indirect transition (DIT) in the bandgap. In comparison to the binary case, where we could use primitive cell for our analysis, in ternary case, however, the proper representations of defects demanded the requirement of relatively large supercell and random structure (SQS) for reasonable statistical significance; both of which together added extra level of difficulties (such as band folding, large project size) in the DIT analysis for ternary systems. At the end, however, using the concept of 'band unfolding' we were able to pinpoint the DIT points with fairly good accuracy for ternary systems[2,3,4]. Subdividing the whole ternary III-V material class into two; presence or absence of defect state inside the 'bandgap' region, further helped us to reduce the project size.

Results

The computational parameters are the same as in reference [1]. There is no DIT for GaAsN within biaxial ± 5 % of strain.

'Bandgap phase diagram'

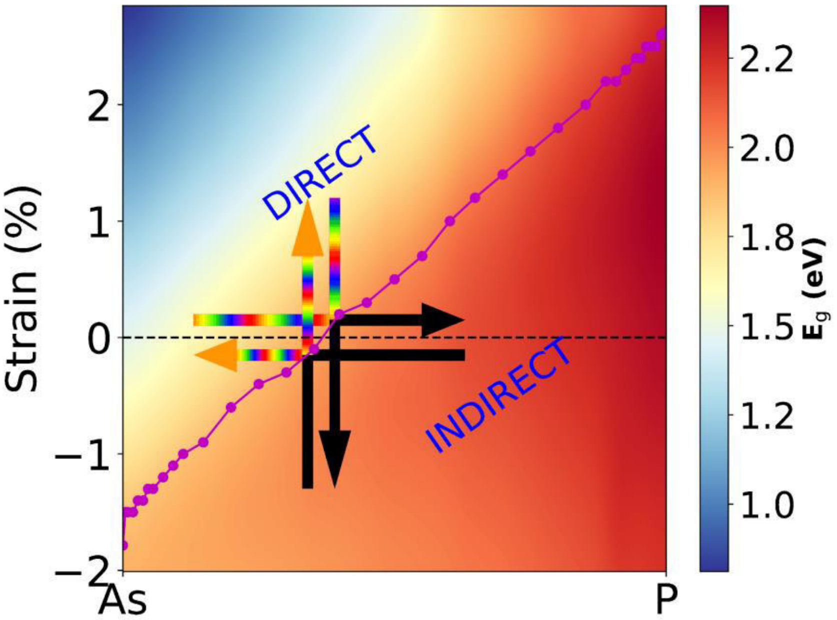

Fig. 1: GaAsP isotropic strain

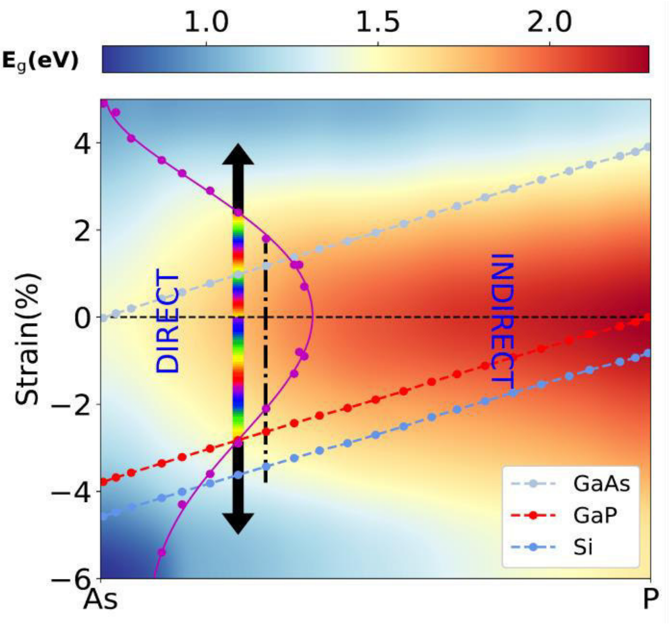

Fig. 2: GaAsP biaxial strain

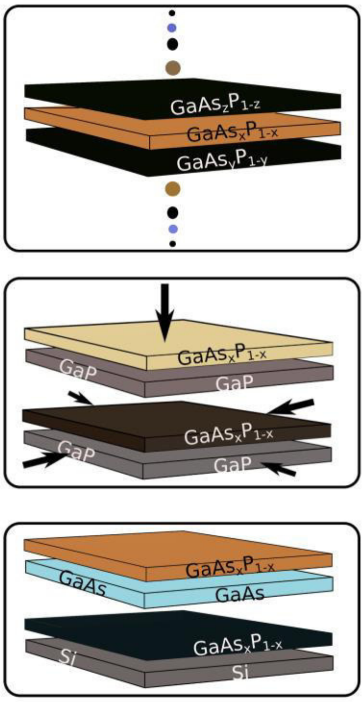

Conclusion

Using *ab-initio* DFT calculation and the idea of 'Bloch spectral function'[2,3,4] we developed a recipe of analyzing the DIT in ternary III-V semiconductor materials which ultimately enabled us to construct the so-called 'phase diagram' of bandgap. As an example case, by applying our recipe we mapped the 'bandgap phase diagram' for two well-known III-V semiconductor materials GaAsP and GaAsN as the model for absence and presence of defect state within the bandgap region, respectively. Although, due to several computational complexity it was not possible to map the full phase diagram for GaAsN, but we tried to cover the most important portion of N concentration in terms of current experimentally achievable limit (final figure is not available yet). With possible applications presented alongside (Fig. 2), we believe that our new way of mapping the effect of strain in III-V ternary (and higher order material) will significantly improve the future development in terms of strategic choice of certain application oriented most suited material system or vice versa.

Outlook

As the future extension of this project we would like to go for higher order material systems for similar and related analysis. As another ambitious goal based on future experimental interest we would like to map different transitions under strain in addition to DIT as well.

References

[1] P. Rosenow et al., Phys. Rev. B 97, 075201 (2018).
[2] L.-W. Wang et al., Phys. Rev. Lett. 80, 4725-4728 (1998).
[3] O. Rubel et al., Phys. Rev. B 90, 115202 (2014).
[4] V. Popescu, A. Zunger, Phys. Rev. B 85, 085201 (2012).

MOVPE growth of Ga(N,As) interlayers with high N contents on GaAs (001) surfaces

O. Maßmeyer, E. Odofin, S. Firoozabadi, T. Hepp, J. Glowatzki, I. Limame,
A. Beyer, K. Volz and W. Stolz

Materials Sciences Center and Department of Physics, Philipps-University Marburg, Germany

Introduction

A large variety of devices and technological applications like LEDs, laser diodes, solar cells, high electron mobility transistors are based on III-V heterostructures grown by MOVPE. A precise control of the interface formation is crucial for realization of these heterostructures. A thorough understanding of the formation and modification of the interface would be beneficial for improvement and realization of new semiconductor devices. With a precise control of the interface formation, e. g. by deposition of a single monolayer of nitrogen, properties like surface morphology, carrier diffusion barriers and hetero offsets in the band structure could be modified.

Results and Conclusions

To modulate the interface, we investigated the growth of very thin Ga(N,As) interlayers containing high amounts of nitrogen on exact, semi-insulating GaAs (001) substrates. Epitaxial growth was conducted in an AIXTRON AIX 200 MOVPE system. For the Ga(N,As) interlayer formation different growth sequences were utilized to realize the most abrupt incorporation by ideally targeting for a monolayer of GaN in the GaAs (001) matrix. A similar approach has been realized before for GaP monolayers grown on GaAs (001) in the same reactor system[1]. As precursors triethylgallium (TEGa), tertiarybutylarsane (TBAs) and 1,1 dimethylhydrazine (UDMHy) were used. The grown structures were monitored in-situ by reflection anisotropy spectroscopy (RAS) to get insight in the surface configuration before, during and after the interlayer growth. The nitrogen concentration and layer thickness were additionally characterized by high-resolution X-ray diffraction (HR-XRD) as well as by scanning transmission electron microscopy (STEM) and the surface morphology of the samples was studied by atomic force microscopy (AFM). For the realization of these thin interlayers different growth sequences were tested. The preliminary determined N incorporation of these structures is shown in Fig. 1. A simple reduction of the growth time using continuous growth (CG) of Ga(N,As) with a growth interruption of 10 s under TBAs and for 10 s under TBAs and UDMHy did not increase the N incorporation compared to the N incorporation of about 4 % in a 5x multi quantum well structure grown with the same parameters. In a second approach we used growth interruptions (GI) with TBAs and UDMHy before and after a short gas pulse of TEGa and UDMHy. This could ideally lead to a very thin layer of GaN. However, our first composition analysis suggests a nitrogen incorporation of 2 to 3 %. The first presumably higher N incorporation was achieved by suppling only UDMHy to the GaAs surface for 1 - 50 s and directly switching to the growth of the GaAs barrier (surface exchange – SE). This leads to a very high effective N/As ratio within the reactor, which should result in a high N incorporation[2]. Furthermore, a pulsed growth (PG) of the interlayer with 1 s TBAs, 0.65 – 2 s TEGa and 2 s UDMHy supply was investigated. The PG also shows a relatively high N incorporation. The PG could result in really thin layers, since a pulse duration of 0.65 s of TEGa is equivalent to roughly one monolayer of Ga on the surface. For the last sequence the TBAs supply was stopped and only TEGa and UDMHy were supplied during the growth of the Ga(N,As) interlayer (GaN sequence). For the GaN sequence a HR-XRD of a sample grown at 525 °C is shown in Fig. 2. The diffractogram clearly shows the interference arising from the repetition of the Ga(N,As) interlayers, which is especially shown in the inset and indicates a good structural quality of the interfaces in the structure. For an additional insight into the grown Ga(N,As) interlayers, quantitative evaluation of the nitrogen content and the layer thicknesses is performed by STEM, which will be discussed in the presentation.

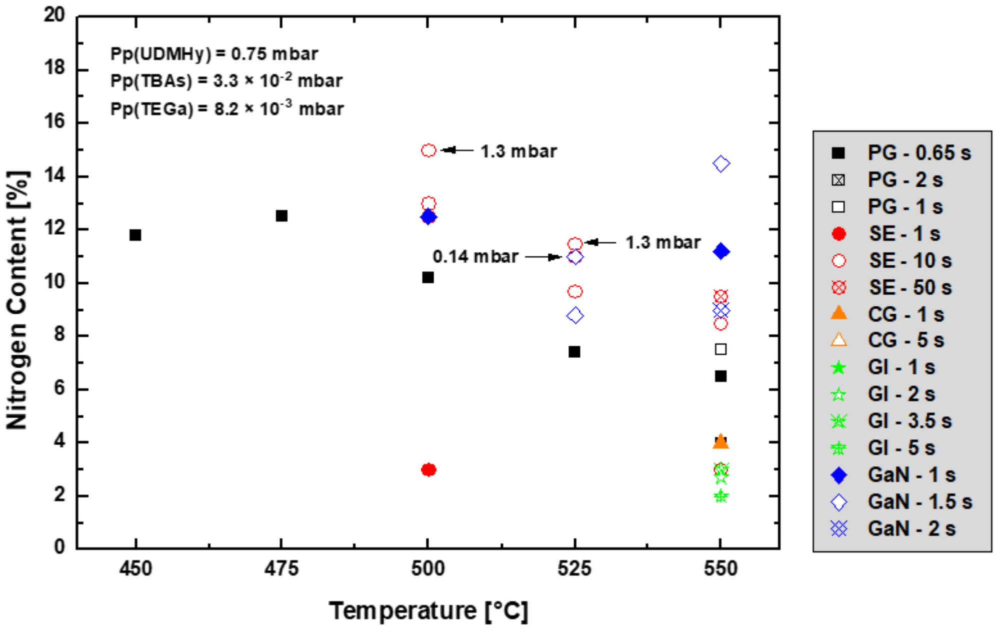

Fig. 1: Summary of the Nitrogen incorporation in the Ga(N,As) interlayers for different growth sequences in dependence of the growth temperature, supply time and UDMHy partial pressure (marked by the arrows). The layer thickness was assumed to be one monolayer (1/2 of a unit cell) for the composition determination, unless the supply time in the respective growth sequence should influence the layer thickness, e. g. in the case of CG with 5 s instead of 1 s.

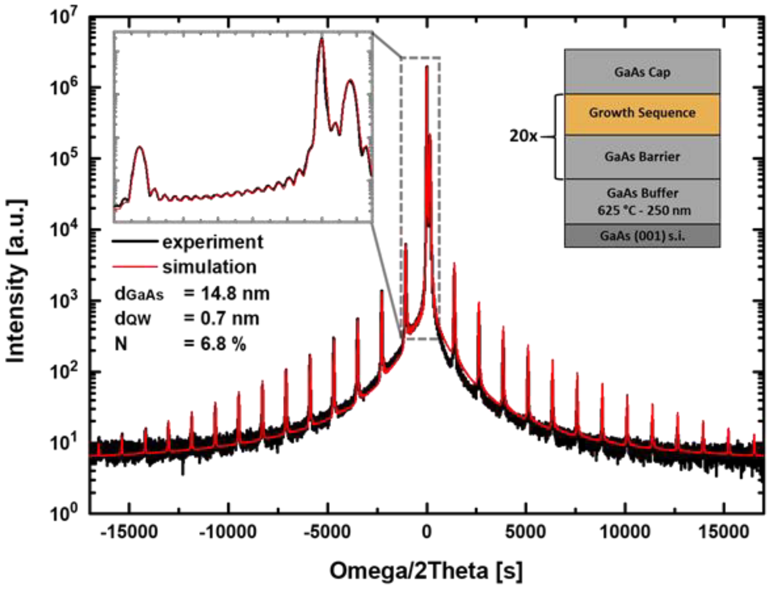

Fig. 2: HR-XRD of an exemplary Ga(N,As) interlayer structure grown on GaAs (001) with the GaN sequence. The insets show a magnification around the substrate peak and the general layer structure.

References

[1] H. Döscher et. al., J. Cryst. Growth, 464 (2017)
[2] K. Volz et. al., J. Cryst. Growth, 311 (2009)

Quantification of light elements at a low angular regime; a combination of EFSTEM and 4DSTEM

S. Firoozabadi, P. Kükelhan, A. Beyer, D. Heimes, J. Lehr, K. Volz

Philipps-University Marburg, Department of Physics and
Materials Sciences Center, Marburg, Germany

Introduction

Composition determination of light elements is in high demand due to their diversity of applications in the fields of electronics, optoelectronics, and batteries. Quantitative scanning transmission electron microscopy (STEM) is one of the most powerful tools for the characterization of nanostructures. It can be achieved by comparing image simulations and experiments at high scattering angles where mainly Rutherford scattered electrons are expected[1]. However, light elements do not scatter efficiently into the scattering angles employed in the z-contrast high angle annular dark-field (HAADF) STEM method. In this study, we establish a method for the composition determination of light elements at a relatively low angular regime. There are sources of discrepancy between image simulations and experimental images especially at low angles such as the influences of amorphous surface layers, inelastic scattering (plasmon excitation), phonon-correlation within the frozen-lattice approach, and distortions in the diffraction plane of the microscope[2,3], which makes the composition determination of light elements disputable. The sources of discrepancy between simulations and experiments at relatively low scattering angles are addressed as follows. We considered SAD by relaxing the supercells before multislice simulations. Energy filtered STEM (EFSTEM) is applied to reduce the effect of plasmon excitations. In the end, a fast pixelated detector is applied, which leads to record the convergent beam electron diffraction pattern (CBED) for every scanning position. Here, with the help of four-dimensional data set, a flexible choice of detection angle is possible to minimize other sources of error. The feasibility of the method is proven by applying it to a simple model material of Si. Then, the composition determination of GaN_xAs_{1-x} QWs is evaluated by the method.

Two samples were investigated in this study: a single-crystalline Si and a sample containing Ga(N,As) quantum well. The latter consists of three GaN_xAs_{1-x} quantum well (QW) structures between GaAs barriers that were grown via metalorganic vapor phase epitaxy (MOVPE) (Aixtron AIX 200 GFR, AIXTRON SE). Each QW layer has a width of 2.7 nm and the nitrogen content is about 4.9 % determined by HRXRD. An electron transparent sample in [010] direction with defined thickness steps is prepared by focused ion beam (FIB) (JEOL JIB-4601F, JEOL Ltd.). Subsequently, the specimen is thinned with low voltage Ar ions using a NanoMill® (Model 1040, E. A. Fischione Instruments). For STEM investigations, a double aberration-corrected STEM JEOL JEM2200FS (JEOL Ltd.) operated at 200 kV and equipped with an in-column Omega energy filter above a pixelated detector (pnCCD (S)TEM Camera, PNDetector) is employed. It allows obtaining energy-filtered (-6 to 6 eV) CBEDs for every probe position. To determine the QWs' composition, complementary image simulations were carried out by STEMsalabim software package[4]. GaN_xAs_{1-x} supercells are created for the expected nitrogen compositions of $x = 0 - 0.1$ and relaxed by the valence force field model.

Results

To prove the feasibility of quantitative agreement between image simulation and experimental data at the low-angular regime, a simple model material of Si is used. The thickness of the sample is determined as 70 nm by the well-established method of STEM-HAADF. Then, CBED patterns as well as position-averaged CBED (PACBED) patterns are recorded applying no energy filtering and zero-loss filtering (**Fig. 1 a**). The elastically scattered PACBED shows more distinct coherent information, i. e., the interference fringes in the {220} discs. To quantitatively investigate the angle-resolved (AR) intensity in each of the unfiltered and elastic signals, the PACBEDs are azimuthally averaged. **Fig. 1 b** depicts the comparison of experimental and simulated AR intensities. Red and blue dashed lines visualize the experimental unfiltered and elastic intensity profiles corresponding to the PACBEDs shown in **Fig. 1 a**. The solid black line belongs to the simulated intensity profile with the thickness derived by HAADF-STEM. Here, due to the energy-filtering of the elastic data, the quantitative comparison of elastic data and the simulations are only achievable by rescaling the filtered data using the ratio between unfiltered and filtered experimental data. It results in the solid blue line, which depicts an excellent agreement with the simulations at angles over 42 mrad while this lower angle limit is 56 mrad for unfiltered data caused by the effect of inelastic scattering at relatively low angles. The deviation at angles below 42 mrad can be explained by neglecting the correlated phonons at simulations, which is an angle-dependent parameter. In the end, the composition determination of GaN_xAs_{1-x} QW is conducted by the combination of EFSTEM and four-dimensional STEM. Here, the optimum detection angle is chosen as 45 to 70 mrad using the same AR analysis applied on Si. Then, the composition is determined according to [5] resulting in the concentration profile in **Fig. 1 d**. In addition, the box-like concentration profile from HR-XRD (red) is shown for comparison. To have a more quantitative comparison the area under the curves is compared. Here, the values derived from EFSTEM and HR-XRD (13.1 % nm vs. 13.8 % nm) yield in a good agreement.

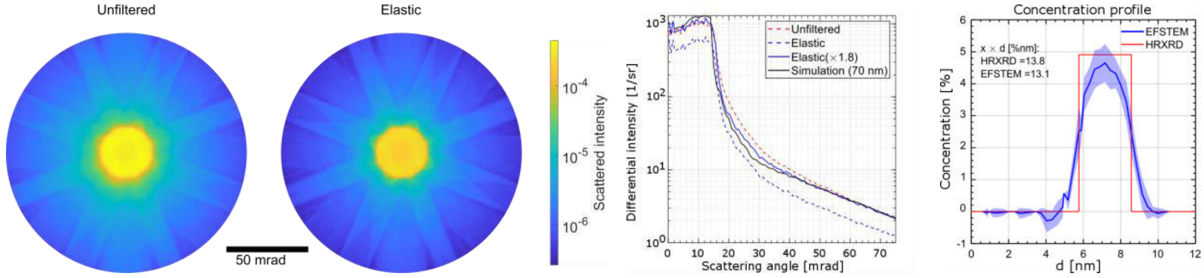

Fig. 1: (a) Unfiltered PACBED and elastically filtered PACBED of Si sample. (b) Differential intensity per solid angle plotted over scattering angle obtained by azimuthal averaging of energy-filtered diffraction patterns (Dashed red: unfiltered; dashed blue: elastic; solid blue: rescaled elastic; black: simulated). (c) Concentration profile derived by EFSTEM using the optimum detection angle.

Conclusions

Facilitated by doing energy-filtered STEM in an optimum angular range, quantitative STEM at low angular regimes is possible. A perfect agreement is obtained between simulations and experiments on the simple model material of Si. In addition, the determined concentration profile yields a good agreement with HR-XRD results.

Outlook

The established method for the quantification of the light elements at relatively low angles can be applied on other light-element-containing material systems such as Lithium-ion batteries.

References

[1] J. M. LeBeau, S. D. Findlay, L. J. Allen & S. Stemmer (2008), Quantitative atomic resolution scanning transmission electron microscopy, *Physical Review Letters*, *100* (20), 206101.

[2] A. Beyer, F. F. Krause, H. L. Robert, S. Firoozabadi, T. Grieb, P. Kükelhan & K. Volz (2020), Influence of plasmon excitations on atomic-resolution quantitative 4D scanning transmission electron microscopy, *Scientific Reports*, *10*, 1-15.

[3] T. Grieb, F. F. Krause, K. Müller-Caspary, S. Firoozabadi, C. Mahr, M. Schowalter & A. Rosenauer (2021), Angle-resolved STEM using an iris aperture: Scattering contributions and sources of error for the quantitative analysis in Si, *Ultramicroscopy*, *221*, 113175.

[4] J. O. Oelerich, L. Duschek, J. Belz, A. Beyer, S. D. Baranovskii & K. Volz (2017), STEMsalabim: a high-performance computing cluster friendly code for scanning transmission electron microscopy image simulations of thin specimens, *Ultramicroscopy*, *177*, 91-96.

[5] L. Duschek, P. Kükelhan, A. Beyer, S. Firoozabadi, J. O. Oelerich, C. Fuchs, W. Stolz, A. Ballabio, G. Isella, K. Volz (2019), Composition determination of semiconductor alloys towards atomic accuracy by HAADF-STEM, *Ultramicroscopy, 200,* 84-96.

High-Harmonic Generation in Tellurium

Sven C. Liebscher, Jörg Hader, Stephan W. Koch

Department of Physics and Materials Sciences Center, Philipps-University Marburg
Wyant College of Optical Sciences, University of Arizona

Introduction

The generation of high harmonics in semiconductor solids by excitation with long-wavelength, short pulses with high field intensities is a field of ongoing research. Since the emission of high harmonics is a result of microscopic dynamics including interband polarizations and intraband currents, it is modeled theoretically using the Semiconductor Bloch Equations (SBE)[1], which account for the microscopic interactions. The excitation of carriers with THz-frequencies is strongly off-resonant and the carriers are accelerated along the bands, so that a treatment of the whole 1. Brillouin Zone (BZ) has to be included. Therefore, the accurate calculation of high harmonic spectra requires detailed knowledge of material parameters. These can be obtained from ab-initio calculations. We use Density Functional Theory together with the shell Local Density Approximation-1/2 (shLDA-1/2) method[2,3] to obtain accurate structural and electronic parameters for use in the microscopic calculations. Tellurium is considered to have exceptional non-linear optical properties[4] due to its chiral structure, forming helical chains. We therefore study its high harmonic generation.

Results

The DFT calculations using the shLDA-1/2 method yield structural and electronic parameters that agree well with experimentally measured values, exhibiting a direct band gap at the H-point of 0.323 eV (exp. 0.33 eV). The resulting bandstructure is shown in Fig. 1. Additionally, the transition dipole matrix elements and the Coulomb matrix elements have been calculated and were used for calculating the absorption spectrum for two polarization directions shown in Fig. 2. Comparison to experimental spectra shows good agreement[5].

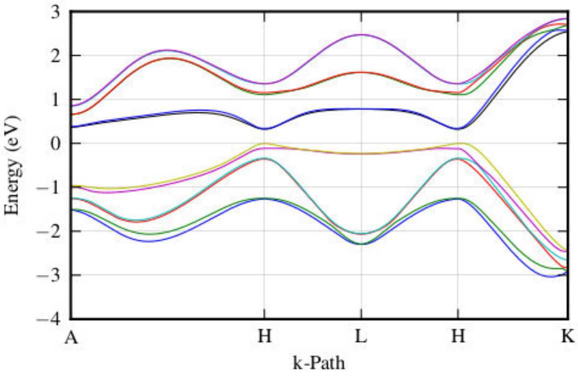

Fig. 1: Bandstructure of Tellurium calculated with DFT using the shLDA-1/2 method.

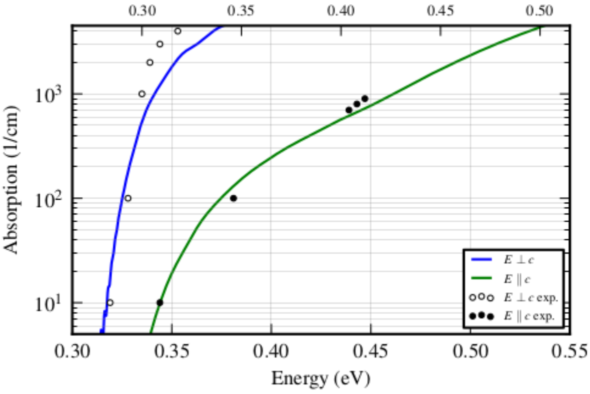

Fig. 2: Absorption spectrum of Tellurium calculated from DFT input data.

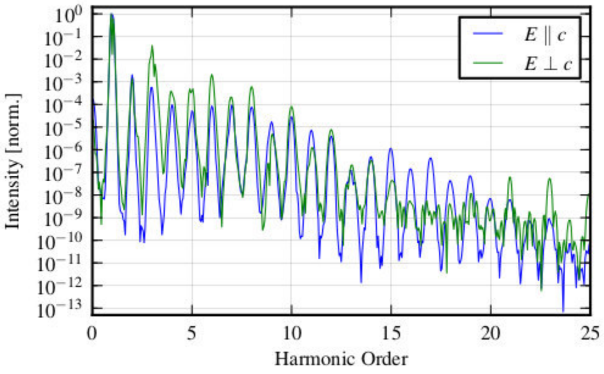

Fig. 3: High-Harmonic spectrum of Tellurium.

Using a microscopic model that includes the non-linear non-perturbative off-resonant excitation of carriers as well as the acceleration of intraband currents, the high harmonic emission of Tellurium was calculated. Resulting emission spectra for excitation with short, strong pulses in two different polarization directions are shown in Fig. 3. The spectrum shows strong harmonics at odd and even orders of the exciting frequency. This is due to the broken inversion symmetry in the crystal, allowing for indirect excitation of carriers into the conduction band.

Conclusions

DFT calculations using the shLDA-1/2 method were performed to accurately describe the material parameters of Tellurium, which were then used in microscopic calculations. The linear and non-linear optical properties of Tellurium have been studied by calculating absorption spectra and high-harmonic emission spectra.

Outlook

Further research will focus on performing the calculations not in a local model, but including propagation effects that arise from the propagation of the field in the material.

References

[1] H. Haug and S. W. Koch, 5th Ed. (World Scientific, Singapore, 2009).
[2] L. G. Ferreira, M. Marques, and L. K. Teles, Phys. Rev. B 78, 125116 (2008).
[3] L. G. Ferreira, M. Marques, and L. K. Teles, AIP Advances 1, 032119 (2011).
[4] V. V. Berezovskii, Y. A. Bykovskii, M. I. Goncharov, and I. S. Rez, Soviet Journal of Quantum Electronics 2, 180 (1972).
[5] R. S. Caldwell and H. Y. Fan, Phys. Rev. 114, 664-675 (1959).

Further research summaries
by RTG-members

(in alphabetical order)

MOVPE Growth and Optimization of Ga(N,As)/Ga(As,Bi)/Ga(N,As) "W"-Type heterostructures for laser applications on GaAs substrate

H. Abouarab[1], T. Hepp[1], R. Günkel[1], W. Stolz[1], S. Chatterjee[2], and K. Volz[1]

[1]Materials Sciences Center and Department of Physics, Philipps-University Marburg, Germany
[2]Institute of Experimental Physics I, Justus-Liebig-University Gießen, Germany

Introduction

The incorporation of Bismuth and Nitrogen into GaAs provides wide scope for band structure engineering with numerous applications for efficient photonic devices operating in the near- and mid-infrared compatible with GaAs substrates[1].

It is observed that the band gap decreases strongly with increasing Bismuth fraction at approximately about 80 to 90 meV per % of Bi[2]. Studies show that the bandgap of the Ga(AsBi) compound with Bi fractions of approximately 10 % is smaller than the spin–orbit splitting with an emission wavelength of 1.55 µm[3]. In addition to the large spin-orbit splitting (ΔS_O) made possible with dilute bismuthide alloys, there have been several reports of large band gap bowing with increasing Bismuth fraction in Ga(As,Bi). This has been attributed to a band anti-crossing interaction between localized Bismuth states and the GaAs valence band edge[4], similar to conduction band anti-crossing that observed in dilute nitride semiconductors such as Ga(N,As). The N incorporation into GaAs up to several percent leads to a significant redshift of the band gap instead of the blueshift[5].

In this work we emphasis on type-II structure, which open up interesting new possibilities in devices design. In such band alignment, the electrons and holes are spatially separated and charge carrier recombination may occur across interface. While it is generally sufficient to stack two quantum wells (QWs) to fabricate a type-II active region, optimizing the structure by embedding a hole QW in between two electron QWs results in an increased wave function overlap[3]. The resulting band structure is sketched in Fig. 1. These heterostructures are referred as "W"-QW heterostructures[6].

Since Bi and N primarily influence the conduction and valence band edges, type-II structures based upon Ga(As,Bi)/Ga(N,As) can be optimized for large wavelength emitting optoelectronic devices[3]. Type-II structures based on Ga(As,Bi)/Ga(N,As) can be fabricated as strain balanced structure, since Bi incorporation introduces compressive strain and N incorporation introduces a tensile strain.

Materials and Experimental

In this part we introduce the MOVPE growth of W-type heterostructures of Ga(N,As)/Ga(As,Bi)/Ga(N,As). The following precursors have been reported as most proper for growing Ga(As,Bi) and Ga(N,As) layers as well[7,8]; triethylgallium (TEGa), tertiarybutylarsine (TBAs), trimethylbismuth (TMBi), and 1,1-dimethylhydrazine (UDMHy) are chosen as Gallium (Ga), Arsenic (As), (Bi) and (N) sources, respectively.

The samples are grown on exact semi-insulating GaAs (001) substrates as shown in Fig. 2. First, a buffer layer is deposited at 625 °C to ensure the same starting conditions for each sample grown. Immediately after deposition of the buffer layer a TBAs stabilized growth interruption is established while reducing the temperature to 550 °C to enable the deposition of Ga(N,As) bulk layers. The growth conditions of Ga(As,Bi) should be carefully chosen to avoid droplet formation[7-9] while increasing Bi incorporation. Particular growth interruption steps are required to obtain the suitable growth condition for each layer. Before the growth of Ga(As,Bi) a Bi wetting is required to suppress a graded incorporation profile. Moreover, the Bi segregation would hinder the Nitrogen incorporation in the second Ga(N,As) QW. Therefore, a Bi desorption is established at 625 °C.

HR-XRD is used to identify thickness and composition of the grown layers, photoluminescence (PL) Spectroscopy is used to determine the bandgap of grown layers. SEM and AFM are used to investigate the interfaces and surface morphology of the grown layers.

Outlook

The 1st aim is to optimize growth conditions for high Bi and N content of around 7 % and 8 %.

The 2nd aim is to study the interfaces of Ga(N,As)/Ga(As,Bi)/Ga(N,As) WQWs. Sophisticated studies of the growth interruptions with varying gas phase composition will be performed while tracking the growth process in-situ using reflection anisotropy spectroscopy.

References

[1] S. J. Sweeney, I. P. Marko, S. R. Jin et al., Bismide-Based Photonic Devices for Near- and Mid-Infrared Applications, in: Bismuth-Containing Compounds (Eds. H. Li, Z. M. Wang), Springer Series in Materials Science 186, Springer, New York (2013), 29 - 53.
[2] P. Ludewig, L. Nattermann, W. Stolz and K. Volz, Semicond. Sci. Technol. 30 (9) (2015), 094017.
[3] C. Broderick, S. Jin, I. P. Marko et al., Sci. Rep. 7 (2017), 46371.
[4] K. Alberi, O. D. Dubon, Appl. Phys. Lett. 91 (2007), 051909.
[5] K. Volz, J. Koch, B. Kunert, I. Németh, W. Stolz, J. Cryst. Growth 298 (2007), 126 - 130.
[6] C. Fuchs, A. Beyer, K. Volz, W. Stolz, J. Cryst. Growth 464 (2017), 201 - 205.
[7] J. Veletas, T. Hepp, F. Dobener, K. Volz, and S. Chatterjee, Appl. Phys. Lett. 118 (5) (2021), 052103.
[8] T. Hepp, O. Maßmeyer, D. A. Duffy, S. J. Sweeney, K. Volz, J. Appl. Phys. 126 (8) (2019), 085707.
[9] P. Ludewig, Z. L. Bushell, L. Nattermann, N. Knaub, W. Stolz, K. Volz, J. Cryst. Growth 396 (2014), 95 - 99.

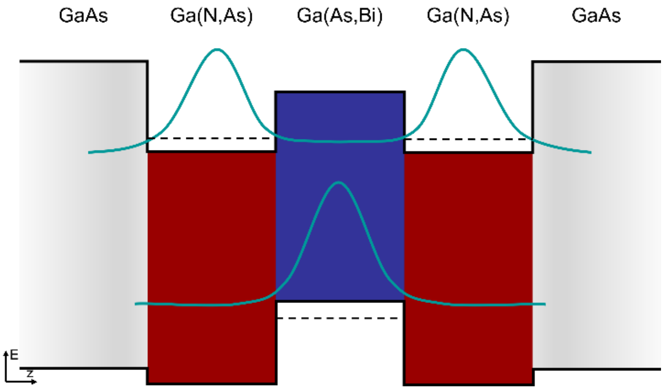

Fig. 1: type-II “W”-quantum well heterostructure consisting of a Ga(AsBi) hole QW embedded in between two (GaN)As electron QWs

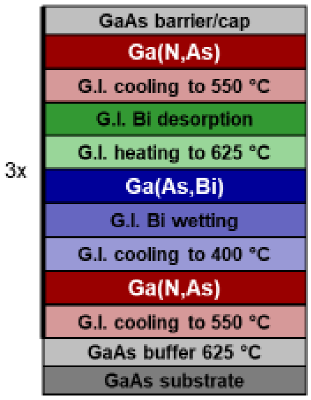

Fig. 2: MOVPE Epitaxial growth for GaNAs/GaAsBi/GaNAs “W quantum well” heterostructure

Controlling Tip-Induced Reaction Products of Surface-Adsorbed Organic Species on Si(001)

Alexa Adamkiewicz[1], Tamam Bohamud[1], Marcel Reutzel[1], Michael Dürr[1,2], and Ulrich Höfer[1]

[1]Department of Physics and Materials Sciences Center, Philipps-University Marburg, Germany
[2]Institute of Applied Physics, Justus-Liebig-University Gießen, Germany

Introduction

Implementing surface chemistry on the nanoscale in the design and fabrication process of miniaturized electronic devices may open a wide range of possible applications. In particular, the functionalization of semiconductor surfaces by means of organic materials, the investigation of the properties of the adsorption process and possible means of manipulating the adsorbates play a crucial role.

Results

Scanning tunneling microscopy and molecular beam studies showed that diethyl ether adsorbs on Si(001) via a datively bound intermediate state[1,2]. Thermal activation ($T > 150$ K) induces C-O cleavage leading to two covalently bound final states, symmetric and asymmetric. In contrast, electronic excitation of the intermediate state was found to lead to a variety of covalently bound final states which are not obtained by thermal activation[3]. This observation is traced back to a release of the steric restrictions which apply for the transition state in the case of thermal excitation. The underlying mechanism of the tip-induced process was found to follow a one-electron excitation scheme with a threshold voltage of $U_{th} \approx 2.5$ V.

Comparing the tip-induced reaction products of surface-adsorbed diethyl ether on Si(001) with the reaction products of tetrahydrofuran on Si(001)[4], which were obtained under equal conditions, allows to study the influence of the geometry of the organic species on the reaction process and the resulting configurations. While the threshold voltage was found to be the same for both species, the reaction products were found to differ in various ways: For one, a configuration which consists of only one molecular fragment was found in the case of diethyl ether. It can be traced back to the desorption or migration of a second fragment. This process was only observed for diethyl ether species while not having a respective counterpart in the number of tip-induced final configurations of tetrahydrofuran adsorbates. This finding can be traced back to the geometric structure of the molecules: While ether cleavage within the frame of a linear geometry (diethyl ether) results in two molecular fragments, the same process leads to only one entity in case of a ring-like arrangement (tetrahydrofuran). As a consequence of the enhanced flexibility of the diethyl ether adsorbates, they are more susceptible to be driven by the surrounding electronic states and their spatial arrangement. This influence can be observed in the remaining reaction products. While the relative positions of the involved Si dimers of each final configuration are alike for both organic species, the actual dimer atom which the entities are bound at may differ. This difference can be traced back to geometrical hindrance in the case of tetrahydrofuran while the diethyl ether entities are more flexible in terms of orientation and spatial alignment and can easily be influenced by the surrounding electronic structure.

Conclusion

Tip-induced electronic excitation of surface adsorbates gives access to new reaction products beyond the thermal excitation scheme. In addition, this study shows that the geometry of the adsorbates plays a significant role in the resulting reaction products.

References

[1] M. Reutzel, G. Mette, P. Stromberger, U. Koert, M. Dürr, and U. Höfer, *J. Phys. Chem. C* **119**, 6018 (2015)
[2] M. Reutzel, M. Lipponer, M. Dürr, and U. Höfer, *J. Phys. Chem. Lett.* **6**, 3971 (2015)
[3] A. Adamkiewicz, T. Bohamud, M. Reutzel, U. Höfer, and M. Dürr, *in preparation*
[4] G. Mette, A. Adamkiewicz, M. Reutzel, U. Koert, M. Dürr, and U. Höfer, *Angew. Chem. Int. Ed.* **34**, 3417 (2019)

Microstructural investigations of Ni-rich Lithium-ion battery layered cathode using High-resolution Scanning transmission electron microscopy

Shamail Ahmed[1], Anuj Pokle[1], Andreas Beyer[1], Jürgen Janek[2], and Kerstin Volz[1]

[1]*Department of Physics and Materials Sciences Center, Philipps-University Marburg*
[2]*Institute of Physical Chemistry & Center for Materials Research, Justus-Liebig-University Gießen*

Introduction

On the way towards a green future, implementing efficient energy storage devices is essential in areas ranging from grid systems through electric vehicles to electronic devices. Lithium-ion batteries (LIB) are amongst the most efficient energy storage devices. Layered cathode materials, for example, lithium cobalt oxide (LCO), lithium transition metal ($Li(Ni_{1-x-y}Co_xMn_y)O_2$) oxide (called NCM), etc., are important class cathode materials used in almost every high-density LIBs that are commercially available. To increase the energy density of LIBs, high Ni (with Ni ≥ 0.6) NCM materials are being investigated because of their practically achievable specific capacities. Ni-rich NCM materials are regarded as the near-term future cathode materials for LIBs.[1] However, Ni-rich NCM layered cathode materials suffer from premature degradation. Since the degradation of cathode materials begins at the nanoscale, understanding such a phenomenon at the atomic scale is inevitable.

Characterizing layered cathode materials is highly challenging due to the polycrystalline nature of secondary particles, their air and moisture sensitivity, and structure and phase transformations complexity. We developed techniques to prepare samples from secondary particles using focused-ion beam (FIB) during this study. We studied the crystal structure extensively and first worked out structural pathways and correlations for the phase transformation through simulating electron diffractions of different crystal phases. We also simulated scanning electron microscopy (STEM) images to find the right zone axis and microscope conditions to characterize these materials efficiently. We also applied the precession electron diffraction (PED) technique to characterize these materials at multiple length scales. We applied the knowledge gained to determine the critical aspect of this class of materials, summarized in the results section.

Results

1. The Role of Intragranular Nanopores in Capacity Fade of Nickel-Rich Layered $Li(Ni_{1-x-y}Co_xMn_y)O_2$ Cathode Materials (ACS Nano, 2019)[2]

NCM degradation, in literature, is mostly explained both by disintegration of secondary particles (large anisotropic volume changes during lithiation/delithiation) and by formation of rock-salt like phases at the grain surfaces at high potential with related oxygen loss. Here, we report the presence of intragranular nanopores in $Li_{1+x}(Ni_{0.85}Co_{0.1}Mn_{0.05})_{1-x}O_2$ (NCM851005) and track their morphological evolution from pristine to cycled material (200 and 500 cycles) using aberration-corrected scanning transmission electron microscopy (STEM), electron energy loss spectroscopy, energy-dispersive X-ray spectroscopy, and time-of-flight secondary ion mass spectrometry. Pores are already found in the primary particles of pristine material. The intragranular pores have a diameter in the range between 10 and 50 nm with a distinct morphology that changes during cycling operation. A rock-salt-like region is observed at the pore boundaries even in pristine material, and these regions grow with prolonged cycling. It is suggested that the presence of nanopores strongly affects the degradation of high-Ni NCM, as the pore surfaces apparently increase (i) oxygen loss, (ii) formation of rock-salt regions, and (iii) strain-induced effects within the primary grains. High-resolution STEM demonstrates that nanopores are a source of intragranular cracking during cycling.

2. Visualization of Light Elements using 4D STEM: The Layered-to-Rock Salt Phase Transition in $LiNiO_2$ Cathode Material (Adv. Energy Mat., 2020)[3]

In this study, we have successfully explored the use of a pixelated detector to image light atoms in the lithium-ion battery cathode active material LNO. A sample was studied for several TEM specimen thicknesses using the HAADF, ABF, and eABF imaging techniques. ABF revealed good sensitivity to lithium and oxygen atoms for small specimen thickness. The contrast of light elements was demonstrated experimentally for the first time to be significantly improved by eABF imaging, especially for larger specimen thicknesses. We also showed that from HAADF-, ABF-, and eABF-images of the same area, specifc insights into phase transformation regions can be gained. The analysis of the layered-to-rock salt phase transition region suggested that there is no sharp interface between the structures. Instead, the transformation appears to take place gradually. In the transition region, no indication for a local structure with spinel symmetry is found. On the other hand, we observed the presence of nickel ions on tetrahedral sites diffusing inwards from the particle’s surface. Oxygen appears to be asymmetrically displaced toward the surface, thereby locally distorting the nickel octahedral environment.

3. A robust technique to image all elements in $LiNiO_2$ cathode active material by 4D-STEM (Microsc. Microanal. Supp., 2021)[4]

4. In Situ Monitoring of Thermally Induced Effects in Nickel-Rich Layered Oxide Cathode Materials at the Atomic Level (ACS Appl. Mater. Interfaces, 2020)[5]

Conclusions

We have developed (and also extending) an electron microscopy ecosystem to characterize the battery materials from nano to atomic-scale during the course of this study.

Outlook

We have planned to extend our analysis and characterize the cathode/solid-state electrolyte (SSE) interface that will be useful for the upcoming (and very promising) all-solid-state batteries (ASSBs) LIBs.

References

[1] A. Manthiram, *ACS Cent. Sci.* **2017**, *3*, 1063.

[2] S. Ahmed, A. Pokle, S. Schweidler, A. Beyer, M. Bianchini, F. Walther, A. Mazilkin, P. Hartmann, T. Brezesinski, J. Janek, K. Volz, *ACS Nano* **2019**, *13*, 10694.

[3] S. Ahmed, M. Bianchini, A. Pokle, M. S. Munde, P. Hartmann, T. Brezesinski, A. Beyer, J. Janek, K. Volz, *Adv. Energy Mater.* **2020**, *10*, 2001026.

[4] S. Ahmed, A. Pokle, J. Belz, M. Bianchini, A. Beyer, J. Janek, K. Volz, *Microsc. Microanal.* **2021**, *27*, 1446.

[5] A. Pokle, S. Ahmed, S. Schweidler, M. Bianchini, T. Brezesinski, A. Beyer, J. Janek, K. Volz, *ACS Appl. Mater. Interfaces* **2020**, *12*, 57047.

Theoretical Analysis of the Optical Properties of W-Laser Structures

A. Bäumner and S. W. Koch

Department of Physics and Materials Sciences Center, Philipps-University Marburg

1. Introduction

Near-infrared semiconductor lasers are the driving force behind the rapid progress in fiber-optic telecommunication. InP-based material systems such as (GaIn)(AsP)/InP have proven to be spectrally suitable choices as active media. However, at high temperatures the performance of these devices is affected by Auger losses and small band offsets compared to materials systems based on GaAs substrate. A potential active medium for semiconductor lasers based on GaAs substrate emitting in the O-band (1.260 µm to 1.360 µm) is the (GaIn)As/Ga(AsSb)/GaAs material system which exhibits a type-II band alignment. The type-II band alignment enables a flexible band structure engineering as well as it offers the possibility to suppress Auger losses. Thus, type-II semiconductor lasers are a promising candidate for more efficient telecommunication lasers. Their fabrication, however, has proven to be challenging. Here, a thorough theoretical description of these type-II heterostructures for actual device applications is beneficial to help understand the relevant processes and make design suggestions.

In type-II heterostructures, electrons and holes are spatially separated in adjacent materials giving rise to an internal electric field that affects the wavefunction overlap of the electron and hole states and thus the device performance. The electron-hole wavefunction overlap is typically improved utilizing so-called **W**-**Q**uantum-**W**ell **H**eterostructures instead of common double quantum wells. These W-QWHs consist of a hole quantum well sandwiched between two electron quantum wells resulting in a “W”-shaped conduction-band alignment and consequently a favourable electron-hole state overlap.

Central components of the many-body theory we use for the analysis of the optical properties of these so called W-laser structures are (i) the 8x8 k·p-theory for the computation of the electronic band-structure, (ii) the well-known semiconductor Bloch equations including the Coulomb-interaction coupling among excitonic excitations for the microscopic description of the linear optical response of a semiconductor material to a classical light-field and (iii) the semiconductor luminescence equations for the description of luminescence resulting from spontaneous recombination of electronic excitations taking into account the quantized light-matter interaction. Together, these equations allow a microscopic, quantitative computation of absorption- and gain spectra, refractive index changes, photoluminescence spectra and intrinsic charge carrier losses caused by radiative and non-radiative recombination processes[1,2].

2. Results

While material gain calculations for (GaIn)As/Ga(AsSb)/GaAs WQWHs are available in literature[3-5], the charge carrier density dependence of the confinement potentials is rarely discussed in detail. In our current analysis, we found that under increasing injected carrier density the band alignment leads to effects that decisively influence the laser performance and are hard to predict without a fully microscopic theory. So, although optical gain spectra of these WQWHs show similar characteristics as type-I heterostructures by reaching transparency and building up significant material gain values as the charge carrier density is increased two important differences may be observed:

Firstly, the material of type-I heterostructures is expected to be red-shifted due to band-gap renormalization as the charge carrier density is increased. The WQWHs under consideration, however, exhibit a characteristic blue shift that is primarily caused by the band bending due to local charge inhomogeneities. Secondly, the material gain spectra are initially dominated by the ground state transition between the e1 and h1 states. However, as the charge carrier density is increased, the transition between the e2 and h2 states slowly starts to contribute. Together, the overlap between e1h1 and e2h2 contributions to the optical gain results in an almost flat gain spectrum over a range of approximately 160 nm at 10.000 x $10^{12} cm^{-2}$.

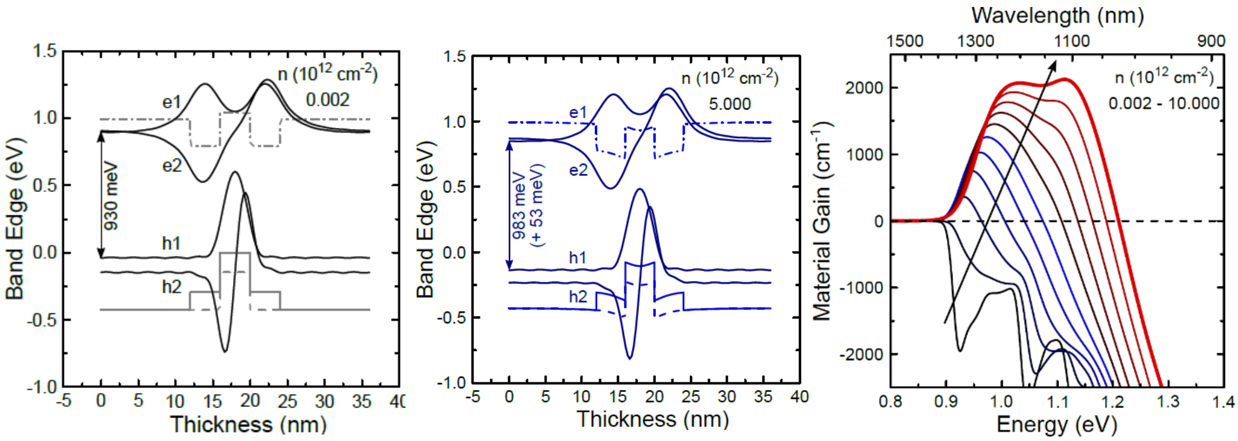

***Figure 1**: Theoretically calculated confinement potentials and functions in the low density regime (left) and for the higher excited device (middle). Theoretically calculated material gain spectra for the WQWH at charge carrier densities between 0.002 x $10^{12} cm^{-2}$ and 10.000 x $10^{12} cm^{-2}$ in steps of 1.000 x $10^{12} cm^{-2}$ (right).*

3. Conclusions

These results highlight the importance of a thorough theoretical analysis and design of WQWHs for actual device applications, because the behavior discussed above may result in in semiconductor lasers switching to higher order transitions under certain operating design of novel semiconductor devises such as optical amplifiers where broad and flat gain spectra are highly beneficial.

4. Outlook

First experiment-theory comparisons of the optical gain spectra for (GaIn)As/Ga(AsSb)/GaAs WQWHs show qualitative good agreement. However, for the high energy side of the spectrum we observe differences in the line shape that indicate decisive inhomogeneous broadening of the experimental results. The theoretical analysis of these inhomogeneous broadening effects is currently work in progress.

5. References

[1] H. Haug and S. W. Koch. Quantum theory of the optical and electronic properties of semiconductors. World Scientific Publishing Company, Fifth Edition, 2009.

[2] W. Chow and S. W. Koch. Semiconductor-laser fundamentals: physics of the gain materials. Springer Science & Business Media, 1999.

[3] W. W. Chow and H. C. Schneider. Charge-separation effects in 1.3 µm GaAsSb type-II quantum-well laser gain. Appl. Phys. Lett., 78 (26): 4100-4102, 2001.

[4] W. W. Chow, O. B. Spahn, H. C. Schneider and J. E. Klem. Contributions to the large blue emission shift in a GaAsSb type-II laser. IEEE J. Quantum Electron., 37 (9): 1178-1182, 2001.

[5] C. Berger, C. Möller, P. Hens, C. Fuchs, W. Stolz, S. W. Koch, A. Ruiz-Perez, J. Hader, and J. V. Moloney. Novel type-II material system for laser applications in the near-infrared regime. AIP Adv., 5 (4): 047105, 2015.

Investigation of the Ultrafast Dynamics of Electronic and Vibronic Excitations at the GaP/Si-Interface

Tim Bergmeier, Gerson Mette

Department of Physics and Materials Sciences Center, Philipps-University Marburg

The charge dynamics at buried semiconductor interfaces are an important factor determining the performance of any device built with semiconductor heterostructures. One of the mechanisms governing charge transfers over said interfaces are coherent interface-specific (IF) phonons, which I want to investigate in heterostructures of GaP/Si(001). These materials serve as a model system for a polar/nonpolar semiconductor heterostructure. Since an acoustic IF-phonon has been found recently[1], I want to identify and characterize an optical IF-phonon with our newly established ultrashort-pulse laser system.

One noninvasive method to investigate the coherent phonons of a semiconductor heterostructure is to measure the linear reflectivity in a pump-probe scheme, with time resolution being achieved by varying the delay between pump- and probe-pulse. By using 45°-polarized light (equal parts s- and p-polarized) as a probe, one can split the probe-beam reflected from the sample into its s- and p-polarized components with a beam-splitter and focus those onto two photodiodes with opposite bias for balanced detection. This method is called electro-optic sampling (EOS) and measures the change in reflected polarization caused by an electric field from the moving atoms of the sample. With this, it is possible to resolve vibrations of higher frequencies compared to measuring only the change in overall reflectivity.

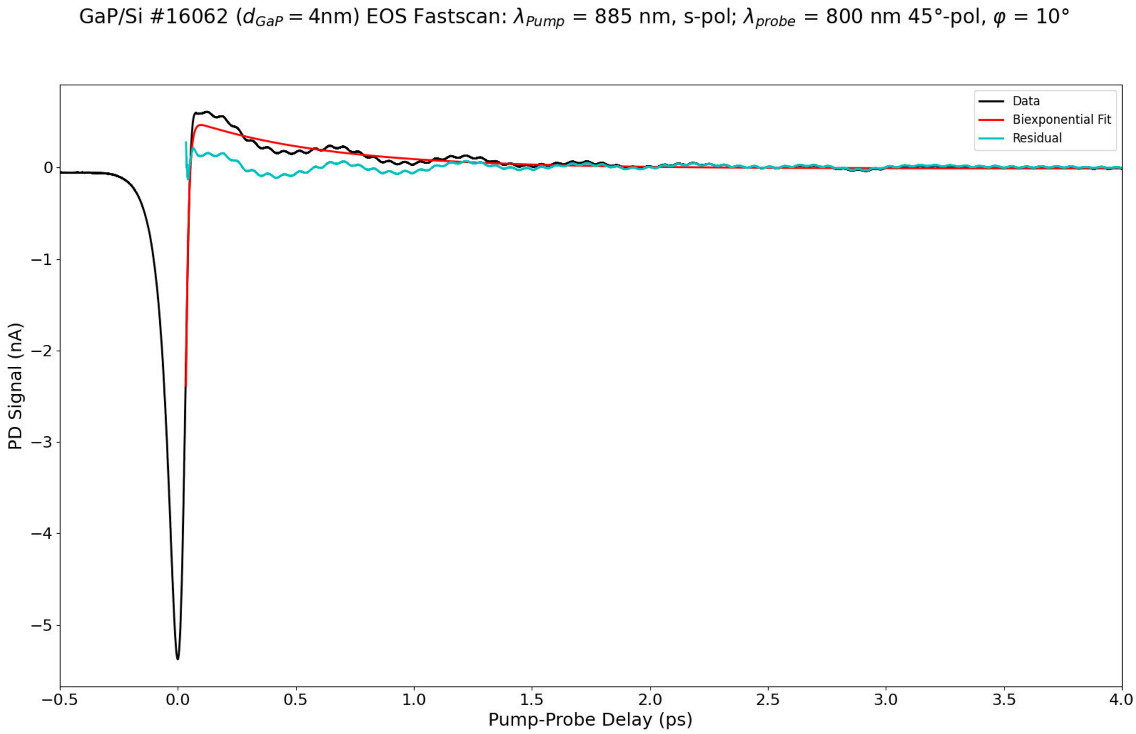

Fig. 1: Time-resolved EOS reflectivity measurement of a GaP/Si(001) sample with s-polarized pump. The biexponantial fit is depicted in red, the oscillating residuum in blue[1].

The resulting time-trace of the reflectivity consists of an initial rise or drop of the signal, depending on whether one uses an s- or p-polarized pump, and afterwards a biexponential decay with the phonon oscillations on top. By fitting to and then subtracting the biexponential decay from the data, one can acquire the oscillating part, which is then analyzed with a fast fourier-transformation (FFT).

I investigated several samples of varying layer thickness, each with the same set of polarization combinations (pump s- and p-polarized and two sample angles with 90° difference).

All samples show the 2 THz low-frequency mode (LFM), while for the samples with pyramidical anti-phase boundaries (APBs)[2], the mode vanishes for a certain pump-polarization with raising GaP-layer thickness. For the ones with straight APBs, the LFM mode is always visible, although in one pump-direction with a lower amplitude.

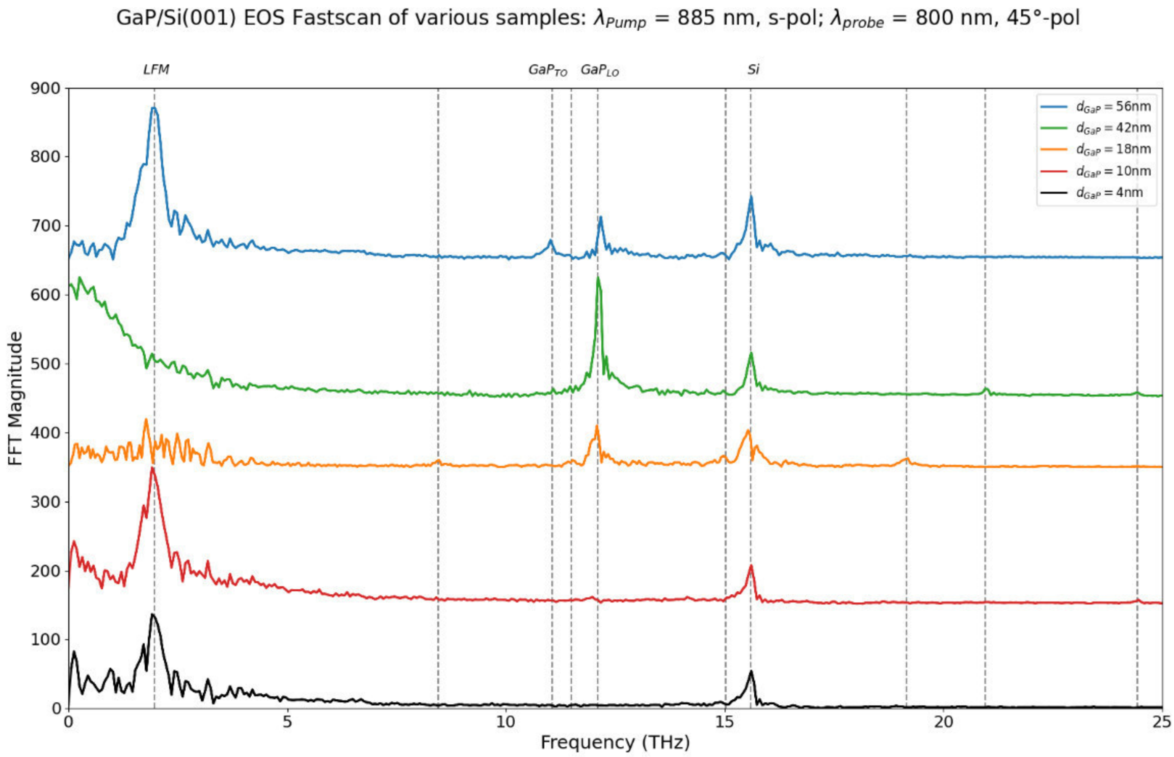

Fig. 2: FFTs of samples with varying GaP layer-thickness. All measurements were done with s-polarized pump, with the sample angle set to the value with the smaller LFM-amplitude. Vertical dotted lines indicate frequencies where a peak is visible for any of the samples.

All FFTs show a peak at the optical phonon mode of Si (15.5 THz), while the GaP LO-phonon mode becomes stronger with raising GaP-layer thickness. The GaP TO-phonon mode only becomes slightly visible for the sample with 56 nm GaP, which also has straight APBs compared to the 42 nm-sample. The most interesting feature is from the 18 nm-sample at 8.45 THz, which could be a potential candidate for the optical IF-phonon, since its frequency is well above the acoustic bulk frequencies and below the optical bulk frequencies of both materials.

In the future, I would like to investigate the origin and behavior of the 8.5 THz peak to determine whether it is an interface phonon or something else, also I would like to compare the results to measurements of samples grown in the (211) direction.

References

[1] K. Ishioka et al., Sub-picosecond acoustic pulses at buried GaP/Si interfaces, Appl. Phys. Lett. **111**, 062105 (2017)

[2] A. Beyer at al., Pyramidical structure formation at the interface between III/V semiconductors and silicon, Chem. Mater. **28**, 3265-3275 (2016)

Scanning Transmission Electron Microscopy Simulations: Improvement and Utilization

Damien Heimes, Andreas Beyer, Saleh Firoozabadi, Jonas Scheunert,
Jürgen Belz, Kerstin Volz

Materials Sciences Center and Department of Physics, Philipps-University Marburg

In order to get quantitative information from scanning transmission electron microscopy (STEM), complementary image simulations are necessary. It is essential that the simulations reproduce the effects which affect the experimental outcome as good as possible. An important part of our work is to improve our simulation codes[1] by including additional effects and also to utilize the code for simulation studies.

Due to the upcoming of fast pixelated detectors it is now possible to capture the whole diffraction pattern in STEM at each scan point instead of only single integrated intensity values as it is done with annular detectors. The two spatial scan dimensions and the two dimensions of the diffraction pattern give 4-dimensional datasets, hence the technique is often called 4-dimensional STEM (4DSTEM).

Electric fields in the specimen deflect the electron beam and lead to a shift in the center of mass (COM) of the diffraction pattern. This shift is approximately proportional to the electric field inducing the shift[2, 3]. Due to this it is possible to measure atomic electric fields[2] and also long-range fields, e. g. of semiconductor homojunctions[4] via 4DSTEM. In one project we introduce long-range electric fields to our simulations in order to be able to predict optimal experimental conditions. This is done by adding the corresponding external potential to the atomic scattering potentials. We can make a direct comparison of simulations with and without the external field and by this make the field's influence visible. This is done for the model system of a GaAs p-n junction. A proof of principle was already given: The p-n junction's field was included in STEM simulations, and the COM shift of the simulated diffraction patterns was measured. The electric field measured from this shift is in very good agreement with the input one. Building up on this, the next steps will be to study the influence of different convergence angles and other parameters on the measurement of the electric field.

In another project we are working on to include the inelastic scattering of electrons in STEM simulations. This is necessary because with increasing specimen thickness, the portion of intensity which goes into the inelastic scattering of electrons increases, and an intensity redistribution in the diffraction pattern occurs[5]. First results show a good qualitative agreement with experiment.

A further current topic is the creation of convolutional neural networks which are able to extract information from experimental 4DSTEM data. For this we create labeled training datasets via STEM simulations. The goal here is to correctly predict the specimen thickness and the tilt out of the crystal axis.

References

[1] J. O. Oelerich et al., Ultramicroscopy 177 (2017): 91-96.
[2] W. Gao et al., Nature 575 (7783) (2019): 480-484.
[3] K. Müller et al., Nature communications 5 (1) (2014): 1-8.
[4] A. Beyer et al., Nano Letters 21 (5) (2021): 2018-2025.
[5] A. Beyer et al., Scientific Reports 10 (2020): 17890.

Automated exploration of reaction networks in chemical vapor deposition by density functional theory

Fabian Pieck[1], Ralf Tonner[1]

[1]University Leipzig, Wilhelm-Ostwald-Institute for Physical and Theoretical Chemistry,
Linnéstraße 2, 04103 Leipzig, Germany

Properties and quality of materials grown by chemical vapor deposition crucially depend on the reactivity of the employed precursor molecules. To study the reactivity of the precursors density functional theory is a convenient tool. Gas phase studies exploring the decomposition of triethylgallane[1], tert-butylphosphine (TBP)[1], trimethyl- and triethylboron[2] and di-tertiary-butyl-arsano-amine[3] already resulted in reaction networks spanning more than 60 elementary reactions. However, a proper model for the whole CVD process (Figure 1) must include the substrate surface. This additional level of complexity promotes the development of automated procedures. Up to date, a variety of approaches exist[4], but they are developed with a focus on gas phase reactions. Therefore, we are developing a systematic and automated procedure to explore the surface reaction network. In this way we can reduce the manual effort and the possibility to miss an important reaction channel. Furthermore, by implementing an efficient Message Passing Interface (MPI) parallelization we can exploit modern high-performance computers.

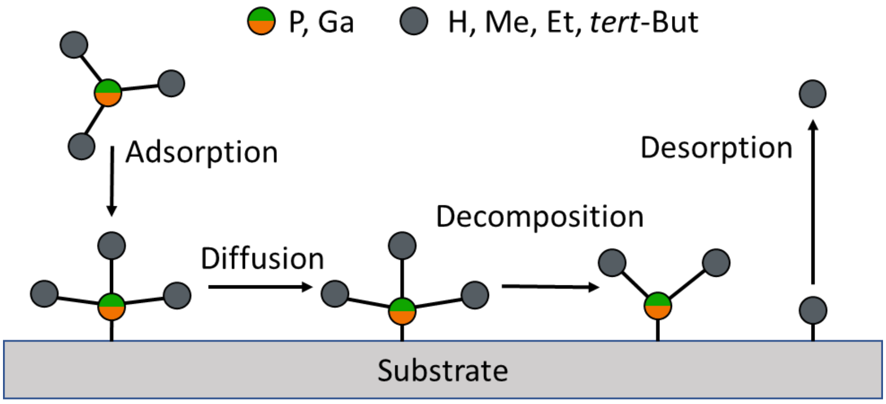

Figure 1: Schematic overview of the elemental steps in the chemical vapor deposition. The surface reaction network consists of energetic minima (structures) and reaction paths connecting the minima (arrows).

Our approach consists of three main steps: In a first step, the adsorption minima for the precursor of interest are calculated. This is achieved in a brute force manner by running a set of structural optimizations in which the molecule is systematically placed above the surface. Linking every observed structure to its final adsorption minimum enables to derive the so-called adsorption basin (Figure 2). We attribute this basin to a probability distribution for the adsorption in a certain minimum. In a second step all decomposition products are created: A distance criterium is used to identify bonded atoms in the precursor. By breaking and rearranging bonds, all decomposition products are formed. In a third step, reaction paths connecting individual structures are automatically selected and calculated. The reaction path optimization is done by a tailored and improved implementation of the nudged elastic band (NEB) method (Figure 3). Here, internal coordinates are exploited for the initial path interpolation. In addition, the NEB is carried out in a serial manner to prevent force evaluations for already converged regions of the reaction path.

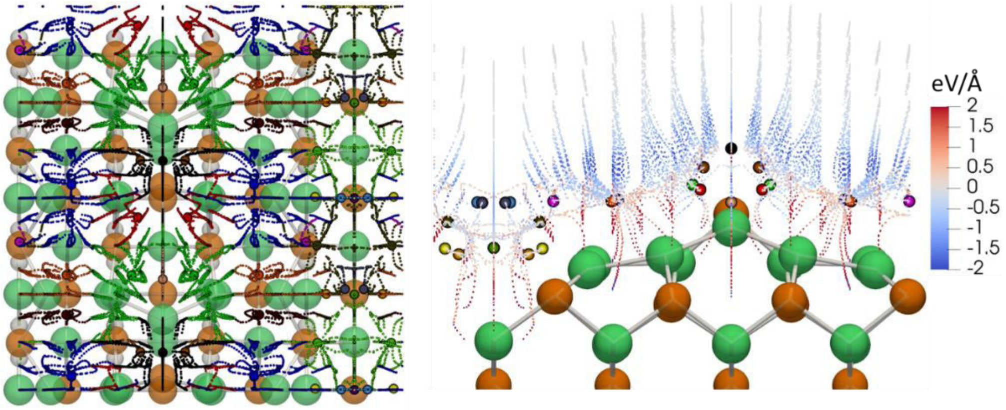

Figure 2: Raw data of the adsorption basin of Bi on GaP(001). In the left figure the data points (small dots) are assigned to their corresponding minimum (larger dots) indicated by the same color. In the right figure the data points are colored corresponding to the force (red: repulsive, blue: attractive) driving the adsorbate to the minimum.

The approach was tested with small model systems like Bi, GaH_3 and PH_3 on GaP(001) and TBP on GaP(001). For the small and computational less demanding model systems our approach could be pushed to its technical limits. For example, the decomposition studies of PH_3 resulted in over 708 k structures contributing to the adsorption basin while 161 diffusion and decomposition paths were computed. For such a work load 16 k cores had to be utilized in parallel. Also, for the computational more demanding TBP our algorithm showed that we can restrict the exploration to a limited number of interesting reactions as the radical cleavage of the tert-butyl group or β-hydrogen elimination reaction. To study the reaction network of molecules like TBP extensively, further improvements in performance and stability will be essential.

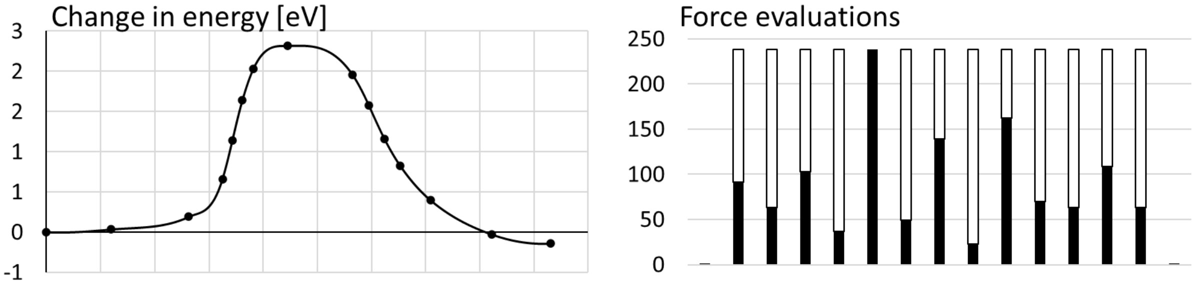

Figure 3: Reaction path of a radical cleavage of TBP on GaP(001). The energy profile (left figure) is sampled by several structures along the reaction path. The transition state is obtained by moving the structure with highest energy in the opposite direction of the gradient. Number of force evaluations per structure are shown in the right figure. The white part of the bars shows the savings due to advanced algorithms.

References

[1] A. Stegmüller, P. Rosenow, R. Tonner, *Phys. Chem. Chem. Phys.* **2014**, *16*, 17018.

[2] a) M. Imam, K. Gaul, A. Stegmüller, C. Höglund, J. Jensen, L. Hultman, J. Birch, R. Tonner, H. Pedersen, *J. Mater. Chem. C* **2015**, *3*, 10898;
b) M. Imam, L. Souqui, J. Herritsch, A. Stegmüller, C. Höglund, S. Schmidt, R. Hall-Wilton, H. Högberg, J. Birch, R. Tonner, H. Pedersen, *J. Phys. Chem. C* **2017**, *121*, 26465.

[3] E. Sterzer, A. Beyer, L. Duschek, L. Nattermann, B. Ringler, B. Leube, A. Stegmüller, R. Tonner, C. von Hänisch, W. Stolz, K. Volz, *J. Cryst. Growth* **2016**, *439*, 19.

[4] a) A. L. Dewyer, A. J. Argüelles, P. M. Zimmerman, *Wiley Interdiscip. Rev. Comput. Mol. Sci.*, **2018**, *8*, e1354;
b) G. N. Simm, A. C. Vaucher, M. Reiher, *J. Phys. Chem. A*, **2019**, *123*, 385-399.

Reactive Solubilization of Heterometallic Clusters by Treatment of $(TrBi_3)^{2-}$Anions (Tr = Ga, In, Tl) with $[Mn\{N(SiMe_3)_2\}_2]$ and $[Zn\{N(SiMe_3)_2\}_2]$

J. Rienmüller, J. Klippstein, G. Werncke, A. Schmidt, F. Weigend, S. Dehnen

Prof. Dr. S. Dehnen, Department of Chemistry and Materials Sciences Center,
Philipps-University Marburg

While Zintl anions are excellent starting materials for the formation of heterometallic and intermetalloid clusters by combining p-block (semi)metal atoms with d- or f-block atoms, their access and handling has been widely limited to highly polar solvents due to their intrinsically high anionic charge. Two strategies to lower the charge and increase the solubility in common organic solvents have been reported in the literature: the addition of organic or elementorganic groups, mostly realized with Zintl anions of group 15 and 14 elements, and the use of Zintl anions like Tt_9^{4-} or Tt_4^{4-} as ligands of transition metal complexes. In the latter cases, the nine- or four-atom cages act as Lewis bases that replace one or more of the original ligands of the transition metal complex.[1-5] So far the products of such reactions with binary Zintl salts lead to very few results, which do not differ from the original Zintl anions regarding their solubility.[6]

The rareness of binary anions with group 13/15 elemental combinations in general,[7-10] but especially the lack of those that are made soluble in common organic solvents through organic shielding, prompted us to develop a new synthetic strategy: shielding of Zintl anions $(TrBi_3)^{2-}$ (Tr = Ga, In, Bi) by low-coordinated transition metal complexes $[M(hmds)_2]$ (M = Mn, Zn; hmds = $N(SiMe_3)_2$) as strong, yet electrochemically inert, electrophiles.

Suspensions of $[K(crypt\text{-}222)]_2(TrBi_3)$ (Tr = Ga, In, Tl) in THF immediately turned dark brown upon addition of $[M(hmds)_2]$, indicating reactive dissolution of the Zintl salt. From these solutions five different crystalline compounds were obtained upon filtration and layering (Fig. 1).

While the $(TlBi_3)^{2-}$ anion remained intact during formation of **1**, the $(GaBi_3)^{2-}$ and $(InBi_3)^{2-}$ anions did not survive the electrophilic attack of $[Mn(hmds)_2]$, despite an entirely analogous reaction. Instead, it decomposed to yield elemental Ga or In, and a Bi_2^{2-} dumbbell, which by varying the bridging of the complex units forms the easily soluble complexes **2**-**4**. Currently the charges of the anions and their magnetic behavior are further investigated.

So far in the reactions with $[Zn(hmds)_2]$ no structures based on Bi_2^{2-} dumbbells were identified. However, from the reaction of $(InBi_3)^{2-}$ an unprecedented Bi_6 unit was crystallized in compound **5**, which represents the $(Bi_6)^{4-}$ backbone of a nortricyclane-type structure that is completed with a $[Zn(hmds)]^+$ unit, and also coordinates a second $[Zn(hmds)]^+$ fragment.

These results indicate a large influence of the transition metal cation on the formation of the products. Therefore, further studies will focus on higher homologues. In addition, the influence of the ligands and their size on the structure of the cluster anions will be investigated.

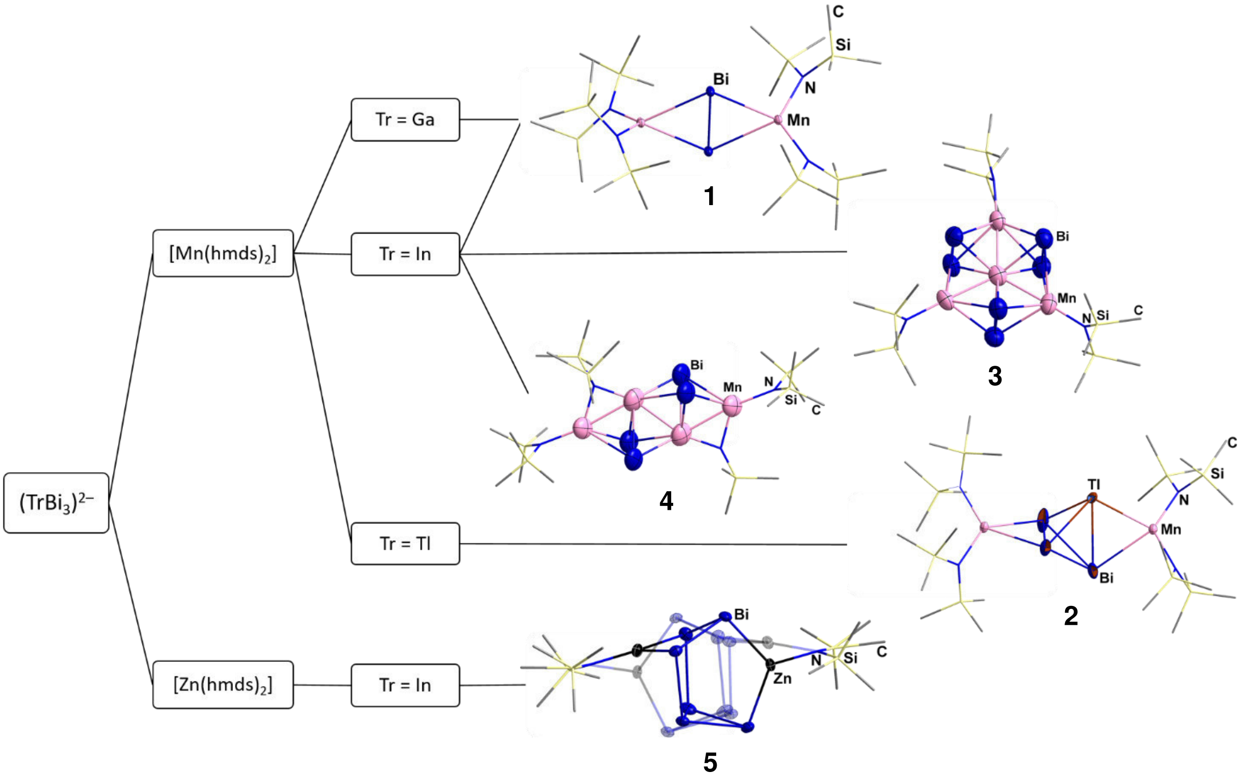

*Fig. 1: Molecule structures of the anions **1**-**5**.*

[1] S. C. Sevov, J. M. Goicoechea, *Organometallics* **2006**, *25*, 5678.
[2] S. Scharfe, T. F. Fässler, *Philos. Trans. Royal Soc. A* **2010**, *368*, 1265.
[3] S. Scharfe, F. Kraus, S. Stegmaier, A. Schier, T. F. Fässler, *Angew. Chem.* **2011**, *50*, 3630.
[4] B. Weinert, S. Dehnen in *Clusters- Contemporary Insight in Structure and Bonding* (Ed.: S. Dehnen), Springer, Berlin, **2017**.
[5] R. J. Wilson, N. Lichtenberger, B. Weinert, S. Dehnen, *Chem. Rev.* **2019**, *119*, 8506.
[6] N. Lichtenberger, N. Spang, A. Eichhöfer, S. Dehnen, *Angew. Chem.* **2017**, *129*, 13436.
[7] N. Lichtenberger, Y. J. Franzke, W. Massa, F. Weigend, S. Dehnen, *Chem. - Eur. J.* **2018**, *24*, 12022.
[8] N. Lichtenberger, W. Massa, S. Dehnen, *Angew. Chem. Int. Ed.* **2019**, *58*, 3222.
[9] A. R. Eulenstein, Y. J. Franzke, N. Lichtenberger, R. J. Wilson, H. L. Deubner, F. Kraus, R. Clérac, F. Weigend, S. Dehnen, *Nat. Chem.* **2021**, *13*, 149.
[10] F. Pan, S. Wei, L. Guggolz, A. R. Eulenstein, F. Tambornino, S. Dehnen, *J. Am. Chem. Soc.* **2021**, *143*, 7176.

Teilnehmer GRK-Seminar

vom 22.09. - 24.09.2021
Tagungshaus Schloss Herborn

In person

Bergmeier	Tim
Dunaj	Tobias
Glowatzki	Johannes
Günkel	Robin
Hepp	Thilo
Kreuter	Florian
Kröner	Marcel
Liebscher	Sven Christian
Ritter	Christian
Rost	Luise
Widemann	Maximilian
Wilhelm	Mikko

Chatterjee	Sangam	Prof. Dr.
Dehnen	Stefanie	Prof. Dr.
Dürr	Michael	Prof. Dr.
Tonner	Ralf	Prof. Dr.
Volz	Kerstin	Prof. Dr.
von Hänisch	Carsten	Prof. Dr.

Virtual

Abouarab	Hanan
Ahmed	Shamail
Firoozabadi	Saleh
Haust	Johannes
Mondal	Badal

Bäumner	Ada	Dr.
Beyer	Andreas	Dr.
Maßmeyer	Oliver	Dr.